Alma Mater Studiorum Università di Bologna
Archivio istituzionale della ricerca

The role of trapped fluids during the development and deformation of a carbonate/shale intra-wedge tectonic mélange (Mt. Massico, Southern Apennines, Italy)

(Article begins on next page)

29 December 2024

1 **The role of trapped fluids during the development and deformation of a**

2 **carbonate/shale intra-wedge tectonic mélange**

3

4 Luca Smeraglia[1,2,3*], Luca Aldega[4], Stefano Bernasconi[5] Andrea Billi[1], Chiara Boschi[6], Antonio

5 Caracausi[7], Eugenio Carminati[1,4], Stefania Franchini[1,4], Andrea Luca Rizzo[7], Federico Rossetti[8],

6 Gianluca Vignaroli[9]

7

8 1. Consiglio Nazionale delle Ricerche, IGAG, c.o. Dipartimento di Scienze della Terra, Sapienza Università di Roma,

9 P.le Aldo Moro 5, 00185 Roma, Italy

10 2. formerly at Dipartimento di Scienze della Terra, Sapienza Università di Roma, P.le Aldo Moro 5, 00185, Roma, Italy

11 3. formerly at Chrono-Environnement, Université de Bourgogne Franche-Comté, 16 Route de Gray, 25000 Besançon,

12 France.

13 4. Dipartimento di Scienze della Terra, Sapienza Università di Roma, P.le Aldo Moro 5, 00185, Roma, Italy

14 5. Geological Institute, ETH Zürich, Sonneggstrasse 5, 8092 Zürich, Switzerland

15 6. Istituto di Geoscienze e Georisorse, Consiglio Nazionale delle Ricerche, Via Moruzzi 1, 56124 Pisa, Italy

16 7. Istituto Nazionale di Geofisica e Vulcanologia, Sezione di Palermo, Via Ugo La Malfa 153, 90146 Palermo, Italy

17 8. Dipartimento di Scienze, Università Roma Tre, Largo San Leonardo Murialdo, 1, 00146, Roma, Italy

18 9. Dipartimento di Scienze Biologiche, Geologiche e Ambientali, BiGeA, Università di Bologna, 40126 Bologna, Italy

19

20 Luca Smeraglia: luca.smeraglia@cnr.it

21 Luca Aldega: luca.aldega@uniroma1.it

22 Stefano Bernasconi: stefano.bernasconi@erdw.ethz.ch

23 Andrea Billi: andrea.billi@cnr.it

24 Chiara Boschi: chiara.boschi@igg.cnr.it

25 Antonio Caracausi: antonio.caracausi@ingv.it

26 Eugenio Carminati: eugenio.carminati@uniroma1.it

27 Stefania Fanchini: stefania.franchini@uniroma1.it

28   Andrea Luca Rizzo: andrea.rizzo@ingv.it

29   Federico Rossetti: federico.rossetti@uniroma3.it

30   Gianluca Vignaroli: gianluca.vignaroli@unibo.it

31

32   *Corresponding author: Dipartimento di Scienze della Terra, Sapienza Università di Roma, Piazzale Aldo

33   Moro 5, 00185 Roma, Italy. Phone +39 06 49914156

34   E-mail address: luca.smeraglia@cnr.it (Luca Smeraglia)

35

36

37

38

39

40

41

42

43

44

45

46

47

48

49

50

51

52

53

54 **Abstract:** In contrast to the numerous studies on exhumed tectonic mélanges along subduction

55 channels, in accretionary wedge interiors, deformation mechanisms and related fluid circulation in

56 tectonic mélanges are still underexplored. Here we combine structural and microstructural

57 observations with geochemical (stable and clumped isotopes and isotope composition of noble

58 gases in fluid inclusions of calcite veins) and geochronological data (U-Pb dating) to define

59 deformation mechanisms and syn-tectonic fluid circulation within the Mt. Massico intra-wedge

60 tectonic mélange, located in the inner part of the central-southern Apennines accretionary wedge,

61 Italy. This mélange developed at the base of a clastic succession, and shear deformation was

62 characterized by disruption of the primary bedding, mixing, and deformation of relicts of competent

63 olistoliths and strata within a weak matrix of deformed clayey and marly interbeds. Recurrent

64 cycles of mutually overprinting fracturing/veining and pressure-solution processes generated a

65 block-in-matrix texture. The geochemical signatures of syn-tectonic calcite veins suggest calcite

66 precipitation in a closed system from warm (108-147 °C) paleofluids, with $\delta^{18}O$ composition

67 between +9‰ and 14‰, such as trapped pore water from diagenesis after extensive ^{18}O exchange

68 with the local limestone host rock ($\delta^{18}O$ values between +26‰ and +30‰) and/or derived by clay

69 dehydration processes (at T > 120 °C). The $^3He/^4He$ ratios in fluid inclusions trapped in calcite

70 veins are lower than 0.1 Ra, hence He was exclusively sourced from the crust, excluding mantle-

71 derived fluids. We conclude that: (1) intraformational rheological contrasts, inherited trapped fluids,

72 and low-permeability barriers such as clay-rich stylolites, can favour the development of fluid

73 overpressure and the generation of intra-wedge tectonic mélanges; (2) clay-rich intra-wedge

74 tectonic mélanges may generate efficient barriers within accretionary wedges for vertical and lateral

75 redistribution of fluids from reservoirs outside the mélange. We highlight that the integration of

76 geochemical and geochronological methods can be a powerful approach to better constrain, in the

77 future, the burial-thermal evolution of fold and thrust belts and sedimentary basins.

78

81

82   **1. Introduction**

83   Décollements and thrust faults are major structures that control the internal architecture of

84   fold-and-thrust belts (e.g. Morley et al., 2017). In particular, décollements commonly generate

85   along evaporite- or clay-rich formations, control the style and timing of folding and tectonic

86   imbrication, and may act as barriers or conduits for crustal flow of fluids, including hydrocarbons.

87   Décollements can often act as channelized paths for fluid redistribution within the crust (e.g.

88   Vrolijk et al., 1988; Vannucchi et al., 2008).

89   The shearing of clay-rich and initially layered formations along décollements can generate

90   tectonic mélanges through primary bedding disruption, pressure-solution, veining, and

91   offscraping/mixing of blocks from competent formations located above and below the décollement

92   horizon (see Festa et al., 2012 for review). Such deformations can lead to block-in-matrix fabrics,

93   consisting of competent blocks scattered in a weak matrix, which are typically characterized by

94   heterogeneous mechanical and permeability properties (e.g. Fagereng, 2011). Outcrop,

95   microstructural, and geochemical characterizations of tectonic mélanges can contribute to constrain

96   their spatio-temporal evolution as well as the mechanical properties and hydrogeological

97   characteristics (paleofluid flow).

98   In this context, several studies focused on tectonic mélanges exhumed from basal

99   décollements at the subduction interface along the toe of accretionary wedges and from subduction

100   channels (e.g. Meneghini et al., 2009; Vannucchi et al., 2008; see Festa et al., 2012 for review),

101   where deformation can reach metamorphic conditions (e.g. Fagereng and Cooper, 2010). Only few

102   studies focused on intra-wedge tectonic mélanges developed at diagenetic P-T conditions along

103   décollements at the base of thrust sheets (e.g. Vannucchi and Bettelli, 2002; Codegone et al., 2012;

104   Dewever et al., 2013; Ogata et al., 2012; Smeraglia et al., 2019). However, intra-wedge tectonic

mélanges may strongly affect the mechanical behavior of inner décollements, thus influencing accretionary wedge geometry and kinematics, and can modulate the transport of fluids (i.e. water, hydrocarbon) across fold-and-thrust belts. Therefore, the understanding of mechanical and hydrological properties of exhumed mélanges is fundamental to unravel fluid (paleo)pathways and asses potential reservoirs for geofluid (i.e. hydrocarbon) accumulation in fold-and-thrust belts.

For these reasons, here we combine outcrop and microstructural observations with geochemical analyses (stable and clumped isotopes and isotope composition of noble gases in fluid inclusions of calcite veins) to unravel the deformation mechanisms, paleohydrology (i.e., fluid conduit/barrier behavior), and the temperature conditions during fluid flow within a 150 m-thick intra-wedge tectonic mélange in the Mt. Massico Ridge (e.g. Billi et al., 1997; Vitale et al., 2018; Smeraglia et al., 2019), which is located in the inner sector (Tyrrhenian side) of the central-southern Apennines fold-and-thrust belt. In this area, outcrop conditions allowed the reconstruction of syn-tectonic paleofluid circulation and the unraveling of progressive intra-wedge mélange deformation, from the undeformed host rock to the finite fabric development by tectonic deformation.

2. Geological background

2.1 Central-southern Apennines

The central-southern Apennines are a late Oligocene to present fold-and-thrust belt generated by the eastward rollback of the west-dipping subduction of the Adriatic plate below the European continental margin (Fig. 1a; e.g., Carminati et al., 2012). Orogenic accretion was accomplished through and accommodated by a set of NE-verging thrust systems, which scraped off pre- and syn-orogenic deposits of the Adriatic plate (Fig. 1b). The pre-orogenic deposits consist of ~4,000-5,000 m-thick Upper Triassic-Middle Miocene carbonate platform deposits (i.e. Apennine platform; e.g. Vezzani et al., 2010; Vitale and Ciarcia, 2018) and of ~100 m-thick middle Miocene hemipelagic marls deposited in a transitional foreland-to-foredeep environment (e.g., Vezzani et al., 2010). The syn-orogenic deposits consist of up to ~3,100 m-thick upper Miocene siliciclastic sandstones, marls,

131 and claystones deposited in a foredeep environment (e.g., Vitale and Ciarcia, 2018). Thrust faults

132 developed during wedge accretion and juxtaposed pre-orogenic deposits onto syn-orogenic

133 sediments, generating stacks of imbricate thrust sheets from the surface down to depths of ~10 km

134 (Fig. 1a,b; e.g. Mostardini and Merlini, 1986; Vezzani et al., 2010). Since early Pliocene time, the

135 internal and axial part of the central-southern Apennines belt underwent tectonic uplift and regional

136 extension, related to the opening of the Tyrrhenian backarc basin and accommodated by the

137 development of NW-SE-oriented extensional faults (Fig. 1a,b; Malinverno and Ryan, 1986).

138

139 *2.2 The Mt. Massico ridge*

140 Mt. Massico is a NNE-SSW-trending ridge located in the innermost part of the central-

141 southern Apennines (Fig. 1a; e.g. Billi et al., 1997; Luiso et al., 2018; Vitale et al., 2018). It is

142 bounded by NE-striking active extensional faults and surrounded by the Quaternary Garigliano and

143 Volturno river plains, the Roccamonfina volcano (Quaternary), and the Tyrrhenian Sea basin (Figs.

144 1a and 2a).

145 In the central and northeastern parts of the Mt. Massico ridge, Upper Triassic to Upper

146 Cretaceous carbonates are exposed (Fig. 1a; Vitale et al., 2018) and arranged to form a ENE-

147 verging asymmetric anticline with an upright forelimb and a WSW-dipping (40°-50°) backlimb

148 (Fig. 1a). In the forelimb, a thrust juxtaposes Upper Cretaceous limestones onto Tortonian syn-

149 orogenic sandstones (see Figure 2 in Sgrosso, 1974). The WSW-dipping backlimb continues in the

150 southwestern part of the ridge, where middle-upper Miocene sediments are exposed (Fig. 2a,b).

151 This succession lies paraconformably atop Upper Cretaceous limestones and begins from the

152 bottom with ~50 m-thick bryozoan-rich limestones of the Cusano Fm., followed upward by

153 hemipelagic marls of the Longano Fm., with a preserved thickness of less than 1-3 meters (Sgrosso,

154 1974; Vitale et al., 2018) (Fig. 2a). Both these formations were deposited in a foreland environment

155 and are Serravallian in age (Sgrosso, 1974). Above the hemipelagic marls, the sedimentary

156 succession evolves into the Tortonian-lower Messinian siliciclastic/carbonaticlastic deposits of the

157 Caiazzo Fm. (hereafter called clastic deposits, Fig. 2a,b), which are interpreted as wedge-top basin

158 deposits (Vitale et al., 2018). The clastic deposits are made up of: (1) massive-to-bedded

159 siliciclastic sandstones with clayey, marly, and calcarenite interbeds and (2) polymictic

160 breccias/conglomerates characterized by Mesozoic-Cenozoic carbonate blocks and siliciclastic

161 clasts (up to a few dm^3 in volume), including also clasts of volcanic, intrusive, and metamorphic

162 rocks (Fig. 2a) (Sgrosso, 1974). The clastic deposits are unconformably overlain by well-bedded

163 lower Messinian calcarenites (Fig. 2a). Intercalated within the clastic deposits are hundreds of

164 olistoliths, from a few dm^3 to several thousands of m^3 in volume. Olistoliths consist of Mesozoic-

165 Cenozoic limestones and exotic rocks not exposed in the local sedimentary succession (hereafter

166 named exotic olistoliths), such as marbles and recrystallized carbonates as well as volcanic,

167 intrusive, and metamorphic rocks, and deep basinal Paleocene limestone blocks (Sgrosso, 1974; Di

168 Girolamo et al., 2000; Vitale et al., 2018). The total thickness of the upper Tortonian-lower

169 Messinian succession is ~800 m (Smeraglia et al., 2019).

170

171 *2.3 The Mt. Massico mélange*

172 The about ~150 m thick basal portion of the clastic deposits and the underlying hemipelagic

173 marls are strongly deformed, showing a block-in-matrix fabric typical of tectonic mélanges (Fig.

174 2a,b; Vitale et al., 2018; Smeraglia et al., 2019). Based on new geological mapping (see also Vitale

175 et al., 2018 for new stratigraphic constraints), structural analysis, U-Pb dating (syn-tectonic calcite

176 ages of 10.5 ± 2.5 My, 7.0 ± 1.6 My, and 5.1 ± 3.7), and thermal modelling constrained by mixed

177 layers illite-smectite, Smeraglia et al. 2019 proposed that the Mt. Massico tectonic mélange

178 developed, since late Messinian times, by out-of sequence thrusting of multiple thrust sheets above

179 the clastic deposits located in the backlimb of the Mt. Massico anticline (Fig. 9a-c) and by

180 localization of deformation at the base of clastic deposits. In this context, the original stratigraphic

181 boundary between the clastic deposits/hemipelagic marls deposits and the underlying limestones

182 was sheared as a décollement horizon and an intra-wedge tectonic mélange developed due to the

183 strong rheological contrast between the weak clastic deposits and the competent limestones. This

184 mélange is characterized by a pervasive S-C and S-CC' fabrics showing a coherent transport

185 direction towards ESE, accommodated by partitioned reverse and dextral transpressive tectonics

186 (Fig. 2a; Smeraglia et al., 2019).

187

188 **3. Methods**

189 Aiming at characterize the structurally-controlled fluid circulation and the geochemical

190 signature of the syn-tectonic fluids in the transition from the undeformed host rock to the tectonic

191 mélange formation, we focused our structural and geochemical studies within the San Sebastiano

192 and Mt. Cicoli areas (Fig. 2). In these areas, it is in fact possible to observe the progressive

193 transition from poorly deformed clastic deposits to moderately and strongly deformed parts of the

194 tectonic mélange along the boundary with the underlying bryozoan-rich limestones of the Cusano

195 Fm. (Fig. 2a). To achieve this purpose we integrated: (1) geological field mapping at 1:10,000

196 scale, and available maps (Billi et al., 1997; Vitale et al., 2018; Smeraglia et al., 2019), to unravel

197 the structural architecture and the deformation history of the intra-wedge tectonic mélange; (2)

198 microstructural (optical microscope) analyses to unravel the deformation mechanisms acting during

199 mélange generation; (3) Stable carbon and oxygen and carbonate clumped isotopes to reconstruct

200 the origin and precipitation temperatures of the paleofluid circulating during mélange generation;

201 (4) H_2O+CO_2, N_2, and minor gaseous species (He, Ne, and Ar concentrations and isotope ratios) in

202 fluid inclusions on previously U-Pb dated syn-tectonic carbonate samples/veins (ages of 10.5 ± 2.5

203 My, 7.0 ± 1.6 My, and 5.1 ± 3.7; Smeraglia et al., 2019) . Sample preparation and analytical details

204 are described in the Supplementary Material.

205

206 **4. Results**

207 *4.1 Outcrop observations*

208   A progressive transition in shear strain localization is observed when moving across strike

209   along the studied area. Within the poorly deformed clastic deposits, bedding is still observable (Fig.

210   3a,b). The competent sandstones beds and the marly-shaly interbeds are gently folded and/or cut by

211   low-displacement reverse faults displaying a ramp-and-flat geometry, with the flat segment located

212   within marly and shaly interbeds (Fig. 3b). The marly and shaly interbeds are characterized by a

213   weak and bedding-parallel scaly foliation (Fig. 3a,b); however, in places, an incipient S-C fabric

214   characterized by bedding-parallel S planes and bedding-oblique C planes occurs dismembering the

215   sandstone interbeds (Fig. 3a).

216   We recognized a up ~100 m-thick zone, referred as moderately deformed zone of the tectonic

217   mélange, exposed within a diffuse boundary between the poorly deformed clastic deposits and the

218   strongly deformed part of the tectonic mélange (Fig. 2). This zone is characterized by still

219   detectable primary structures such as bedding, but competent strata (i.e. sandstones and calcarenites

220   interbeds) show pinch-and-swell and boudin-like geometries. Pervasive and anastomosing bedding-

221   parallel scaly foliation occurs within marly and shaly interbeds (Fig. 3c,d) and, in places, S-C

222   fabrics can be observed (Fig. 3e). With increasing deformation, primary foliation is dismembered

223   and relicts of bedding are scattered within the scaly foliation generating a block-in-matrix fabric

224   (Fig. 3d-e). In particular, such relicts show bedding-perpendicular calcite veins (Fig. 3d,e).

225   The strongly deformed part of the tectonic mélange, up to ~50 m-thick, shows well-developed

226   S-C and S-CC' tectonites and sedimentary structures are completely obliterated by tectonic fabric

227   (Figs. 3f-h and 4a,b). In particular, the WNW- to WSW-dipping S- and C-surfaces show dip angles

228   ranging ~60°-70° and ~10°-30°, respectively, with kinematic indicators showing mainly reverse

229   dip-slip to right-lateral transpressional movements (Fig. 2a). Marls and shales are affected by S-C

230   foliations and clasts of competent rocks (i.e. sandstones and calcarenites) are deformed in

231   sigmoidal-lozenge-shaped structures consistent with the overall sense of shear (Figs. 3f-g and 4a-c).

232   Stylolites and slickenfibers are aligned parallel respect to S and C planes, respectively, whereas

233   sigmoidal clasts of competent rocks are permeated by calcite veins (Figs. 3g,h and 4d).

234   With increasing deformation, the sigmoidal relicts of sedimentary structures are progressively

235   thinned and completely obliterated by S-C foliation so that it is difficult to distinguish them from

236   the pervasive scaly foliation at the naked eye (Fig. 4c). In places, foliated marls and shales wrap

237   olistoliths inherited from clastic deposits. The olistoliths preserve their original (from irregular to

238   rounded) shapes, generating a block-in-matrix fabric (Fig. 4e-g). Convolute/contorted foliations

239   also occur (Fig. 4h). Their origin is not clear and it cannot be excluded that they may be relicts of

240   soft sediment (fluid escape) structures. When observable, the boundary between the tectonic

241   mélange and the underlying bryozoan-rich limestones (not affected by deformation and with

242   sedimentary structures and fossils still recognizable) is sharp.

243

244   *4.2 Microstructural observations*

245   We focused our microstructural observations on the strongly deformed parts of the tectonic

246   mélange, with special focus on the sigmoidal-lozenge clasts of competent rocks (i.e. sandstones and

247   calcarenites), since they are cohesive and can be easily cut for thin section preparation.

248   The sigmoidal-lozenge clasts are characterized by pervasive stylolites, parallel to S, C, and C'

249   planes (Fig. 5a-c). Stylolites evolve from rough, teeth-shaped, and indented morphology (Figs. 5a-c

250   and 6a-b) to smooth, continuous, and thick (up to 1 mm) dissolution seams (Figs. 5a-c and 6c) filled

251   by insoluble material (i.e. clay minerals and oxides), small clasts of host rock limestones, and

252   fragments of calcite veins (Fig. 6c). Stylolites and dissolution seams bound sigmoids defining a

253   fabric sub-parallel to S, C, and C' planes (Figs. 5a-c and 6a,b). Sigmoids consist of host rock

254   commonly with deformed microfossils, and/or reworked calcite veins (Fig. 6a,b).

255   We identify fibrous and blocky calcite veins. Fibrous veins are oriented perpendicular to

256   stylolites ad are characterized by fibrous crystals perpendicular to vein margins (Fig. 6 d-f).

257   Crystals are deformed by stylolites (Figs. 6d-f and 7a). The slickenfibers observed at the outcrop

258   scale along S, C, and C' planes are characterized, at the microscale, by fibrous veins located along

259   stylolite jogs, characterized by fibrous crystals parallel to stylolites (Fig. 6b,f). In places, fibrous

260 veins occur within thick dissolution seams (Fig. 7a,b). In this case, vein margins and fibrous

261 crystals are roughly parallel and perpendicular to dissolution seam margins, respectively (Fig. 7a,b).

262 Blocky veins are filled by blocky to elongated-blocky calcite crystals and are oriented parallel,

263 perpendicular, or oblique to stylolites (Fig. 7c,d).

264   Concerning the relative timing of structures, we observed mutual crosscutting relationships

265 between veins and stylolites (Figs. 5c and 7f). In particular, blocky veins perpendicular to stylolites

266 cut or are deformed by stylolites and/or by blocky/fibrous veins oriented oblique to stylolites (Figs.

267 5 and 7c-f). Fibrous veins parallel and/or perpendicular to stylolites are deformed by stylolites

268 and/or by blocky veins oriented oblique to stylolites (Figs. 5, 7a,b, and 6d-f)

269

270 *4.3 Stable and clumped isotopes*

271   Results from stable and clumped isotopes analyses are shown in Fig. 8 and listed in Table S1

272 and S2. Results are reported in the conventional δ notation with respect to the Vienna Pee Dee

273 Belemnite (VPDB) for $\delta^{13}C$ and Vienna Standard Mean Ocean Water (VSMOW) $\delta^{18}O$ for

274 Clumped isotopes are reported in the Carbon Dioxide Equilibrium Scale (Dennis et al. 2011).

275   The host rock $\delta^{13}C$ and $\delta^{18}O$ values, measured on limestones interbeds within clastic deposits,

276 range between -0.5‰ and +1.5‰, and between +26‰ and +29.5‰, respectively. Such values are

277 typical of Miocene marine carbonates in the Apennines, Italy (e.g., Hilgen et al., 2005).

278   Blocky veins $\delta^{13}C$ and $\delta^{18}O$ values range between 0‰ and +0.8‰ and between +22.3‰ and

279 +27‰, respectively, with one blocky vein showing $\delta^{13}C$ and $\delta^{18}O$ values overlapping those of the

280 host rock. Fibrous veins $\delta^{13}C$ and $\delta^{18}O$ values range between -0.4‰ and +1.6‰ and between

281 +22.4‰ and +27.8‰, respectively. Three fibrous veins show $\delta^{13}C$ and $\delta^{18}O$ values overlapping

282 those of the host rock. Overall, both blocky and fibrous veins show $\delta^{13}C$ values overlapping with

283 those of the host rock and an average $\delta^{18}O$ depletion of ~4‰ respect to the host rock.

284   Clumped-isotope data from blocky veins (four samples) and fibrous veins (five samples)

285 yields $\Delta47$ values between 0.424 and 0.482 (Table S2). These values correspond to temperatures

286   between 108 ± 13 °C and 147 ± 20 °C (Fig. 8b and Table S1), using the equation of Bernasconi et

287   al. (2018). The calculated $\delta^{18}O$ paleofluid compositions, using the O'Neil et al. (1969) equation

288   developed for calcite precipitation temperature in the 0-500 °C range, range between 9.1‰ and

289   13.7‰ (Fig. 8b and Table S1).

290

291   *4.4 Noble gas analysis*

292   The concentrations of CO_2+H_2O, N_2, light noble gases (He, Ne, Ar), and $^3He/^4He$, $^4He/^{20}Ne$,

293     $^{40}Ar/^{36}Ar$ isotopic ratios in fluid inclusions hosted in syntectonic calcite veins (samples 239, 257

294   and 260) are reported in Table S3.

295   CO_2+H_2O and N_2 show concentrations ranging between 1.1×10^{-6} and 8.3×10^{-6} mol/g and

296   between 3.1×10^{-7} and 6.7×10^{-7} mol/g, respectively. The N_2/Ar ratios range between 3092 and 3633.

297   These values are much more higher than the N_2/Ar ratio in the atmosphere (84.1) and the N_2/Ar

298   ratio in air-saturated water at standard temperature and pressure (38). The $^{40}Ar/^{36}Ar$ ratios vary from

299   367.3 to 389.9, slightly higher than the $^{40}Ar/^{36}Ar$ ratio in atmosphere (298.6).

300   He/Ar and He/N_2 ratios range between 0.06-0.14 and $2.1-3.8 \times 10^{-5}$, respectively, and are 1-2

301   orders of magnitude higher than the theoretical values in the atmosphere and in the air-saturated

302   water. The $^4He/^{20}Ne$ ratios range between 51.7 and 96.5 and are more than two orders of magnitude

303   higher than the typical $^4He/^{20}Ne$ ratio in air saturated water (0.268), consistently with fluids trapped

304   at great depth. All these ratios testify an excess of He and N_2 respect to the typical concentrations in

305   atmosphere-derived fluids. The $^3He/^4He$ ratios, corrected for the air contamination (R/Ra ratio)

306   range between 0.05 and 0.09, consistently with those of crustal fluids, thus excluding a contribution

307   of He derived from atmospheric air and ^3He from the mantle (Fig. 8d).

308   The $^3He/^4He$ and $^{40}Ar/^{36}Ar$ ratios are useful tracers to ascertain the origin of the fluids

309   producing the mineralization. However, one condition is that these materials must contain volatiles

310   trapped during precipitation processes and that their isotopic compositions have not been modified

311   over time. Significant post precipitation processes that may affect the noble gases content in the

312   fluid inclusions regard the addition of (1) ^{4}He, ^{40}Ar produced from the radiogenic decay of U, Th

313   and K, and (2) cosmogenic ^{3}He derived from the exposure to cosmic ray.

314   In order to estimate the contribution of radiogenic ^{40}Ar into the fluid inclusions, we computed

315   the ^{40}Ar*, which is the amount of ^{40}Ar corrected for the atmospheric contributions (^{40}Ar* =

316   ^{40}Ar/^{36}Ar$_{Measured}$ - ^{40}Ar/^{36}Ar$_{Atmosphere}$ x ^{36}Ar$_{Measured}$). The amounts of ^{40}Ar* range between 8.99 x 10^{-11}

317   to 1.38 x 10^{-10} mol/g (Table S3). The amounts of the measured ^{4}He and measured ^{40}Ar* do not

318   show any correlations with the ages of the veins (Fig. S1a,b), thus excluding the accumulation of

319   radiogenic He and Ar produced in the veins by the U, Th and K decay during time.

320   All calcite veins have been collected in outcrops whose time of exposure to the cosmic ray at

321   the surface is not evaluable; hence, the potential contribution of cosmogenic ^{3}He trapped in the fluid

322   inclusions is difficult to be assessed. However, there is no correlation between the amount of ^{3}He

323   and the ages of calcite veins (Fig. S1c), which can supports a progressive accumulation over time of

324   cosmogenic ^{3}He and subsequent migration into the fluid inclusions.

325   On the basis of the average U and Th amounts in the veins of calcite (1.58 and 2.28 ppm for

326   sample 257; 0.35 and 0.01 ppm for sample 239; 0.17 and 0.02 ppm for sample 260; Table S4) is

327   possible to compute the potential ^{4}He/^{40}Ar* ratio produced by the decay of U and Th. The

328   computed ^{4}He/^{40}Ar* ratios range between 10 and 100. These values are much higher than the same

329   ratios in the fluid inclusions (0.61, 0.35, and 0.40 for samples 257, 239, and 260, respectively, Table

330   S3). This suggests that the fluid inclusions are not modified by the contributions of both of

331   radiogenic ^{4}He and ^{40}Ar produced within the rocks. We conclude that the isotopic ratios of He and

332   Ar in the fluid inclusions are representative of the pristine isotopic signatures of the trapped fluids.

333

334   **5. Discussion**

335   *5.1 Mélange evolution and deformation mechanisms*

336   Since late Messinian times, the Mt. Massico tectonic mélange developed by out-of sequence

337   thrusting of multiple thrust sheets above the clastic deposits and by localization of deformation at

338   the base of clastic deposits (Fig. 9a-c; Smeraglia et al., 2019). Therefore, when out-of sequence

339   deformation initiated, WSW-ENE shortening affected W-SW-dipping (30°-55°) Meso-Cenozoic

340   carbonates and middle-upper Miocene clastic deposits, tilted by previous thrust-related folding (Fig.

341   2a,b and 9b; Smeraglia et al., 2019). In this context, both layer-perpendicular/oblique shortening

342   and layer-parallel extension occurred in the early phases of deformation (Fig. 10a,b). Layer-

343   perpendicular/oblique shortening was driven by sub-horizontal tectonic compression and produced

344   bedding-parallel foliation by pressure-solution and stylolites generation in the marly and shaly

345   interbeds (Figs. 3a,b). Layer-parallel extension produced dismembering, boudinage, and fracturing

346   of competent bedding (i.e. sandstones and calcarenites interbeds; Fig. 3c).

347   With increasing deformation, the hemipelagic marls between the clastic deposits and

348   bryozoan-rich limestones were scraped off and mixed within the base of clastic deposits, the

349   competent beds were almost completely dismembered, although some relicts of bedding were

350   scattered within the shaly/marly matrix (Figs. 3d, 4e-g, and 10c,d). In this framework, S-C

351   tectonites and block-in-matrix fabric developed within the strongly deformed parts of the tectonic

352   mélange by brittle-ductile processes such as pressure-solution, fracturing/veining, and frictional

353   sliding, with absence of evident cataclasis of the host rock (Fig. 10c,d). The absence of cataclasis is

354   related to the occurrence of widespread pressure solution processes, triggered and enhanced by

355   clay-rich host rocks (marls and shales; Renard et al., 1997), which promoted the dissipation of

356   tectonic stress through host rock dissolution, at slow strain rates rather, than frictional processes

357   (i.e. fracturing, grain rotation, abrasion) commonly occurring during cataclasis in competent rocks,

358   such as pure carbonates (e.g. Billi, 2010). In particular, pressure-solution was more pervasive in

359   weak marly and shaly interbeds than in calcarenite interbeds, producing a network of stylolites

360   aligned along S, C, and C' planes. Stylolites developed through host rock dissolution and insoluble

361   materials (i.e. mainly phyllosilicates) concentrated within dissolution seams (Figs. 3f-h and 4a-c)

362   (e.g. Tesei et al., 2013). Fracturing/veining processes, coupled with pressure-solution, affected the

363 relicts of competent rocks (Figs. 3f-h, 4a-d, and 10c,d). These types of deformation mechanisms

364 commonly occur during tectonic mélange generation (e.g., Festa et al., 2012 for review).

365

366 *5.2 Vein development within the mélange*

367 The occurrence of veins perpendicular to stylolites suggests that both structures formed under

368 the same stress regime, characterized by compression sub-perpendicular to the stylolites, thus

369 generating mode I vein opening perpendicular to stylolites to regulate their evolution through time

370 (Figs. 5a-c, 6d, 7c-f, and 11; e.g., Gratier et al., 2013). Veins parallel to stylolites (Figs. 6f and 7a,b)

371 indicate opening direction parallel to the maximum compression direction and suggests vein

372 opening under an unfavorable stress regime (i.e. opening direction should be perpendicular with

373 respect to the maximum principal stress). In particular, development of fibrous veins (shear

374 veins/slickenfibers) characterized by fibrous crystals perpendicular to the maximum principal stress

375 have been observed in tectonic mélange and have been related to shear along pre-existing weak

376 planes such as clay-rich stylolites, assisted by fluid overpressure (Fagereng et al., 2010).

377 Alternatively, the unfavorable orientations between veins and tectonic stresses can be explained by

378 episodic stress rotation within the mélange, vein reworking/rotation during deformation, and/or

379 overpressured fluids that may have opened pre-existing discontinuities, such as stylolites. Although

380 stylolites are commonly considered efficient barriers to fluid flow (Toussaint et al., 2018 for

381 review), veins developed along stylolites (Fig. 7a,b) suggest that they can be preferential pathways

382 for fluid redistribution, consistently with recent experimental and field evidence (e.g., Heap et al.,

383 2014; Bruna et al., 2019). In particular, the low-permeability network generated by stylolites can

384 favor fluid overpressure rise.

385 Stylolite steps filled by calcite crystals (Fig. 6f) suggest opening of voids (i.e. extensional

386 pull-apart) due to slip along undulated stylolites, which promoted calcite precipitation into newly

387 created space, a mechanism commonly occurring during slickenfiber generation (e.g. Fagereng and

388 Byrnes, 2015). This mechanism indicates that frictional sliding occurred along S-, C-, and C'-planes

389 by smoothing the tooth-shaped margins of stylolites and slip along thick clay-rich dissolution seams

390 (Fig. 10d; Tesei et al., 2013).

391   Fibrous crystals (Figs. 6d-f and 7a,b) generated through multiple and micrometer-thick

392 opening increments (e.g., Bons et al., 2012), is incompatible with coeval growth of blocky and/or

393 elongated-blocky crystals that typically develop in fluid-filled spaces generated by a single opening

394 increment larger than that of fibrous veins (e.g. Bons et al., 2012). These different deformation

395 mechanisms suggest various slip rates and deformation behaviors within the mélange. Continuous

396 deformation may have occurred within the ductile clay-rich matrix, while discontinuous slip may

397 have occurred during fibrous and blocky vein generation in more competent carbonate-rich blocks

398 (e.g. Fagereng, 2011). In particular, fibrous veins suggest discontinuous creep at very slow slip

399 rates. On the contrary, impulsive deformation at high and fast slip rates may have occurred during

400 blocky vein generation generated by impulsive crackle-like brecciation (e.g. Woodcock et al., 2014;

401 Fagereng and Byrnes, 2015). In both cases, fracturing/veining were probably assisted by fluid

402 overpressure, consistently with crackle-like brecciation (Fig. 5) and the dense network of clay-rich

403 stylolites, which may have created impermeable barriers and fluid pressure rises over time (Moore

404 and Vrolijk, 1992).

405   Crosscutting relationships between structures show recurrent cycles of mutually overprinting

406 brittle (fracturing/veining and frictional sliding) and ductile (pressure-solution) processes indicate a

407 multiphase deformation history (Figs. 5, 6, 7, and 11). Stylolite formation through fibrous veins

408 (Fig. 6d,e) indicate the interruption of the fracturing event and the onset of a new pressure-solution

409 phase, indicating alternating phases of frictional sliding and dissolution processes (Fig. 11; e.g.,

410 Tesei et al., 2013; Giorgetti et al., 2016). Reworking of inherited veins also occurred (Figs. 10b and

411 11). This inference is consistent with previous U/Pb dating on three calcite-filled veins within the

412 tectonic mélange showing ages of 10.5 ± 2.5 My, 7.0 ± 1.6 My, and 5.1 ± 3.7 My, respectively

413 indicating multiple events of calcite precipitation during deformation (Smeraglia et al., 2019).

414

415   *5.3 Fluid source and syn-tectonic fluid circulation*

416   Geochemical data indicate calcite precipitation at temperatures between ~100 and ~150 °C

417   from retained pore water, such as marine water retained in the clastic sediments during diagenesis,

418   modified or completely buffered by isotope exchange with the host rock. We base this interpretation

419   on the following evidence:

420   (1) The calculated $\delta^{18}O$ paleofluid composition, which was in equilibrium with the calcite at

421   the time of mineral growth, ranges between +9.1‰ and +13.7‰ (Fig. 8b). These values indicate

422   ^{18}O enrichment suggesting extensive oxygen exchange between the fluids and the limestone

423   interbeds of clastic deposits. In particular, most of the calculated $\delta^{18}O$ paleofluid compositions

424   ranging between +9‰ and +11‰ (Fig. 8b), indicate high water/rock ratios and paleofluids with

425   nearly constant $\delta^{18}O$ composition, which were responsible for calcite precipitation at progressive

426   increasing temperatures from 108 to 146 °C (Fig. 8b).

427   (2) Data from fluid inclusions in veins suggest an excess of radiogenic He and Ar in fluids

428   circulating during the precipitation of calcite, indicating a source of both He and Ar other than the

429   atmosphere and the mantle. In particular, the $^{3}He/^{4}He$ ratios are lower than 0.1 R/Ra (Fig. 8d and

430   Table S3) indicating a crustal fluid. In addition, these values are similar to those of crustal-derived

431   fluids (with limited or negligible mantle contribution) enriched in ^{4}He recorded in natural gaseous

432   emissions of the central-northern Apennines (e.g., Buttitta et al., 2020).

433   (3) The R/Ra ratios of calcite veins are lower than those calculated from actual springs along

434   the Mt. Massico ridge and related to the Roccamonfina volcano (0.39 Ra to 1.99 Ra, typical of

435   mantle-derived fluids; Cuoco et al., 2017), located ~20 towards the NE respect to the study area

436   (Fig. 1), thus excluding the contribution of mantle-derived fluids circulating within the tectonic

437   mélange. In addition, the volcanic activity at Roccamonfina occurred between ~0.6 and ~0.1 My,

438   ~5 My after the latest tectonic activity documented at Mt. Massico (U-Pb vein dated at 5.1 ± 3.7

439   My, Smeraglia et al., 2019), further excluding the mixing of mantle-derived fluids from

440   Roccamonfina with crustal fluids circulated within the tectonic mélange.

441 However, we cannot completely exclude that also meteoric water partly infiltrated within the

442 tectonic mélange during deformation and/or exhumation, and was modified by ^{18}O isotope

443 exchange with the host rock, acquiring the calculated $\delta^{18}O$ paleofluid composition.

444 Based on geochemical and geological data, we suggest that syn-tectonic fluid circulation

445 within the Mt. Massico mélange occurred in a closed system, without a strong connection with

446 external reservoirs (i.e. meteoric or mantle-derived fluids). We therefore propose that during

447 sedimentary and tectonic burial, marine-derived fluids trapped within sandstones and shale

448 interlayers were progressively heated up to 147 °C. During deformation, regional tectonic

449 shortening caused sandstones and shale compaction, porosity reduction, and, eventually, expulsion

450 of previously stored fluids and calcite precipitation into newly-created fractures. In addition, the

451 progressive smectite to illite conversion through mixed layers illite-smectite occurring from

452 temperatures of 60-70 °C to 210 °C (Aldega et al., 2017), may have triggered additional source for

453 local fluids due to water expulsion during clay dehydration (e.g. Moore and Vrolijk, 1992).

454 Syn-tectonic fluid circulation in closed systems has been already observed in tectonic

455 mélange exposed in various fold-and-thrust belts (i.e. Apennines, Pyrenees) developed within

456 sedimentary succession with alternating of sandstones, marls, and shale (e.g., Vannucchi et al,

457 2010; Gabellone et al., 2013; Lacroix et al., 2014). The Mt. Massico mélange did not acted as a

458 conduit for external fluids as observed within intra-wedge tectonic mélange in the Apennines

459 (Meneghini et al., 2012), Sicilian (Dewever et al., 2013), Thailand (Hansberry et al., 2015), and

460 Japan (Raimbourg et al., 2015) fold-and-thrust belts. We explain this difference suggesting that

461 meso- and microstructures of the Mt. Massico mélange, such as clay-rich stylolites and marls-shale

462 interlayers (Figs. 3, 4, 6, and 7), created efficient low-permeability barriers, which prevented the

463 ingress of fluids from external reservoirs. Otherwise, the occurrence of regional thrusts, both below

464 and above the Mt. Massico tectonic mélange, may have acted as regional conduits for the drainage

465 of external fluids within the accretionary wedge and away from the tectonic mélange.

466   We observe an inverse correlation between fluid temperature and ages of calcite veins,

467   showing an increase of calcite precipitation temperature with decreasing ages (Fig. 8c; U-Pb data

468   from Smeraglia et al., 2019). The vein formed at 10.5 ± 2.5 My at temperature of 108 °C suggests

469   an early phase of deformation during wedge accretion (e.g. Tavani et al., 2015). This is not

470   consistent with the burial history proposed by Smeraglia et al. (2019), which shows much lower

471   temperature for the base of the clastic deposits than that recorded by clumped isotopes before the

472   onset of thrusting at 10.5 ± 2.5 My (i.e. Tortonian time; see Fig. 13a in Smeraglia et al., 2019). This

473   can be explained by the lateral and upward migration of deep-seated warm fluids, previously stored

474   in areas already affected by tectonic burial (e.g., Minshull et al., 1989), which circulated within the

475   clastic deposits at shallow depths during the Tortonian. The occurrence pre-Tortonian tectonic

476   burial is highlighted by the borehole stratigraphy of Mara 01 well, located towards the SW respect

477   the Mt. Massico, showing the thrusting of Triassic deposits above Paleocene-Eocene deposits (See

478   Fig. 2 in Smeraglia et al., 2019)

479   Veins formed at 7.0 ± 1.6 My and 5.1 ± 3.7 My at temperatures of 121 and 147 °C,

480   respectively, are consistent with the progressive burial due to thrust sheet emplacement above the

481   mélange (Smeraglia et al., 2019). However, we point out that most of precipitation temperatures are

482   fully consistent with the maximum burial temperature of 140 °C at depths of ~4 km experienced by

483   the mélange, calculated by 1D thermal modelling constrained by mixed layers illite-smectite

484   (Smeraglia et al., 2019). This indicates that fluid expulsion occurred under maximum burial

485   condition, suggesting that tectonic overburden promoted and/or triggered fluid overpressure and

486   hydrofracturing.

487

488   **Conclusions**

489   Structural and microstructural observations combined with geochemical data (stable and

490   clumped isotopes and isotope composition of noble gases in fluid inclusions of calcite veins) along

491 the carbonate/shale-bearing tectonic mélange within the central Apennines accretionary wedge (Mt.

492 Massico mélange) show that:

493 (1) Intra-wedge tectonic mélange generates along pre-existent intra- and interformational

494 rheological contrast occurring along carbonate/shale sedimentary successions. In particular,

495 deformation is localized at the boundary between weak (Tortonian clastic deposits and hemipelagic

496 marls) and competent (Meso-Cenozoic limestones) rocks. The development of tectonic mélange

497 occurred by disruption of the primary bedding, mixing, and deformation of relicts of competent

498 blocks (i.e., olistoliths and relicts of competent strata) within a weak matrix (i.e., deformed shaly

499 and marly interbeds), through recurrent cycles of mutually overprinting brittle (fracturing/veining

500 and frictional sliding) and ductile (pressure-solution) processes, indicating a polyphase deformation

501 history characterized by fast to slow strain rates.

502 (2) The geochemical signatures of syn-tectonic calcite veins indicate calcite precipitation

503 from warm (108-147 °C) and modified pore fluids, by isotope exchange with the local host rock.

504 Fluid circulation occurred mostly in a closed system dominated by the expulsion and redistribution

505 of pore fluids trapped during sedimentation/diagenesis and/or derived by clay dehydration processes

506 (at T > 120 °C), without the interaction of externally derived fluids (i.e. meteoric and/or mantle-

507 derived fluids). A minor contribution from lateral-upward migration of deep-seated warm fluids,

508 previously stored in areas affected by tectonic burial located towards the SW from the Mt. Massico,

509 is inferred in the early phase of the deformation of tectonic mélange. Low-permeability barriers,

510 generated by clay-rich stylolites, promoted the generation of fluid overpressure, which were mostly

511 expelled at maximum burial conditions (T 140 °C and depth of ~4 km) in the final stage of mélange

512 deformation. Therefore, clay-rich intra-wedge tectonic mélanges, along décollement zones, may

513 generate efficient barriers within accretionary wedges for vertical and lateral redistribution of fluids

514 from reservoirs outside the mélange.

515

516   We highlight that the integration of geochemical (stable and clumped isotopes, analysis of

517   gaseous species in fluid inclusions) and geochronological (U-Pb dating) methods can be a powerful

518   approach to better constrain the burial-thermal evolution and the fluid storage capacity of fold and

519   thrust belts and sedimentary basins, including the associated fault network.

520

528

529   **References**

530   Aldega L., Carminati E., Scharf A., Mattern F. & Al-Wardi M. (2017). Estimating original

531   thickness and extent of the Semail Ophiolite in the eastern Oman Mountains by paleothermal

532   indicators. *Marine and Petroleum Geology, 84*, 18-33.

533   Bernasconi, S. M., Müller, I. A., Bergmann, K. D., Breitenbach, S. F., Fernandez, A., et al. (2018).

534   Reducing uncertainties in carbonate clumped isotope analysis through consistent

535   carbonate-based standardization. *Geochemistry, Geophysics, Geosystems*, *19*(9), 2895-2914.

536   Billi, A. (2010). Microtectonics of low-P low-T carbonate fault rocks. *Journal of Structural

537   Geology*, *32*(9), 1392-1402.

538   Billi, A., Bosi, V., & De Meo, A. (1997). Caratterizzazione strutturale del rilievo del M. Massico

539   nell'ambito dell'evoluzione quaternaria delle depressioni costiere dei fiumi Garigliano e

540   Volturno (Campania settentrionale). Il Quaternario, 10(1), 15–26.

541 Bons, P. D., Elburg, M. A., & Gomez-Rivas, E. (2012). A review of the formation of tectonic veins

542 and their microstructures. *Journal of Structural Geology*, *43*, 33-62.

543 Bruna, P. O., Lavenu, A. P., Matonti, C., & Bertotti, G. (2019). Are stylolites fluid-flow efficient

544 features?. *Journal of Structural Geology*, *125*, 270-277.

545 Buttitta, D., Caracausi, A., Chiaraluce, L., Favara, R., Morticelli, M. G., & Sulli, A. (2020).

546 Continental degassing of helium in an active tectonic setting (northern Italy): the role of

547 seismicity. *Scientific Reports*, *10*(1), 1-13.

548 Carminati, E., Lustrino, M., & Doglioni, C. (2012). Geodynamic evolution of the central and

549 western Mediterranean: Tectonics vs. igneous petrology constraints. Tectonophysics,

550 579, 173–192. https://doi.org/10.1016/j.tecto.2012.01.026

551 Codegone, G., Festa, A., & Dilek, Y. (2012). Formation of Taconic mélanges and broken

552 formations in the Hamburg Klippe, central Appalachian orogenic belt, eastern Pennsylvania.

553 *Tectonophysics*, *568*, 215-229.

554 Cuoco, E., Minissale, A., Tamburrino, S., Iorio, M., & Tedesco, D. (2017). Fluid geochemistry of

555 the Mondragone hydrothermal systems (southern Italy): water and gas compositions vs.

556 geostructural setting. *International Journal of Earth Sciences*, *106*(7), 2429-2444.

557 Dennis, K. J., Affek, H. P., Passey, B. H., Schrag, D. P., & Eiler, J. M. (2011). Defining an absolute

558 reference frame for 'clumped' isotope studies of CO2. *Geochimica et Cosmochimica Acta*,

559 *75*(22), 7117-7131.

560 Dewever, B., Swennen, R., & Breesch, L. (2013). Fluid flow compartmentalization in the Sicilian

561 fold and thrust belt: Implications for the regional aqueous fluid flow and oil migration history.

562 *Tectonophysics*, *591*, 194-209.

563 Di Girolamo, P., Sgrosso, I., De Gennaro, R., & Giurazzi, S. (2000). Metamorphic rocks in

564 Campania (southern Italy); The "Mondragone marbles". Bollettino della Societa Geologica

565 Italiana, 119(3), 761–766.

566   Fagereng, Å. (2011). Fractal vein distributions within a fault-fracture mesh in an exhumed

567   accretionary mélange, Chrystalls Beach Complex, New Zealand. *Journal of Structural*

568   *Geology*, *33*(5), 918-927.

569   Fagereng, Å., & Byrnes, G. (2015). A range of fault slip styles on progressively misoriented planes

570   during flexural-slip folding, Cape Fold Belt, South Africa. *Journal of Structural Geology*, *70*,

571   156-169.

572   Fagereng, Å., & Cooper, A. F. (2010). The metamorphic history of rocks buried, accreted and

573   exhumed in an accretionary prism: An example from the Otago Schist, New Zealand. Journal

574   of Metamorphic Geology, 28(9), 935–954. https://doi.org/10.1111/j.1525-1314.2010.00900.x

575   Fagereng, Å., Remitti, F., & Sibson, R. H. (2010). Shear veins observed within anisotropic fabric at

576   high angles to the maximum compressive stress. *Nature Geoscience*, *3*(7), 482.

577   Festa, A., Dilek, Y., Pini, G. A., Codegone, G., & Ogata, K. (2012). Mechanisms and processes of

578   stratal disruption and mixing in the development of mélanges and broken formations:

579   Redefining and classifying mélanges. *Tectonophysics*, *568*, 7-24.

580   Gabellone, T., Gasparrini, M., Iannace, A., Invernizzi, C., Mazzoli, S., & D'antonio, M. (2013).

581   Fluid channeling along thrust zones: the Lagonegro case history, southern Apennines, Italy.

582   *Geofluids*, *13*(2), 140-158.

583   Giorgetti, C., Collettini, C., Scuderi, M. M., Barchi, M. R., & Tesei, T. (2016). Fault geometry and

584   mechanics of marly carbonate multilayers: An integrated field and laboratory study from the

585   Northern Apennines, Italy. *Journal of Structural Geology*, *93*, 1-16.

586   Gratier, J. P., Thouvenot, F., Jenatton, L., Tourette, A., Doan, M. L., & Renard, F. (2013).

587   Geological control of the partitioning between seismic and aseismic sliding behaviours in

588   active faults: Evidence from the Western Alps, France. *Tectonophysics*, *600*, 226-242.

589   Hansberry, R. L., Collins, A. S., King, R. C., Morley, C. K., Giże, A. P., Warren, J., ... & Hall, P. A.

590   (2015). Syn-deformation temperature and fossil fluid pathways along an exhumed detachment

591   zone, khao khwang fold-thrust belt, Thailand. *Tectonophysics*, *655*, 73-87.

592 Heap, M. J., Baud, P., Reuschlé, T., & Meredith, P. G. (2014). Stylolites in limestones: Barriers to
593   fluid flow?. *Geology*, *42*(1), 51-54.

594 Hilgen, F., Aziz, H. A., Bice, D., Iaccarino, S., Krijgsman, W., Kuiper, K., ... & Zachariasse, W. J.
595   (2005). The global boundary stratotype section and point (GSSP) of the Tortonian stage
596   (Upper Miocene) at Monte Dei Corvi. *Episodes-Newsmagazine of the International Union of*
597   *Geological Sciences*, *28*(1), 6-17.

598 Lacroix, B., Travé, A., Buatier, M., Labaume, P., Vennemann, T., & Dubois, M. (2014).
599   Syntectonic fluid-flow along thrust faults: Example of the South-Pyrenean fold-and-thrust
600   belt. *Marine and Petroleum Geology*, *49*, 84-98.

601 Luiso, P., Paoletti, V., Nappi, R., La Manna, M., Cella, F., Gaudiosi, G., & Iorio, M. F. M. (2018).
602   A multidisciplinary approach to characterize the geometry of active faults: The example
603   of Mt. Massico, Southern Italy. Geophysical Journal International, 213(3), 1673–
604   1681. https://doi.org/10.1093/gji/ggy080

605 Malinverno, A., & Ryan, W. B. (1986). Extension in the Tyrrhenian Sea and shortening in the
606   Apennines as result of arc migration driven by sinking of the lithosphere. Tectonics,
607   5(2), 227–245. https://doi.org/10.1029/TC005i002p00227

608 Meneghini, F., Marroni, M., Moore, J. C., Pandolfi, L., & Rowe, C. D. (2009). The processes of
609   underthrusting and underplating in the geologic record: Structural diversity between
610   the Franciscan Complex (California), the Kodiak Complex (Alaska) and the Internal
611   Ligurian Units (Italy). Geological Journal, 44(2), 126–152. https://doi.org/10.1002/gj.1144

612 Meneghini, F., Botti, F., Aldega, L., Boschi, C., Corrado, S., Marroni, M., & Pandolfi, L. (2012).
613   Hot fluid pumping along shallow-level collisional thrusts: the Monte Rentella Shear Zone,
614   Umbria Apennine, Italy. *Journal of Structural Geology*, *37*, 36-52.

615 Minshull, T., & White, R. (1989). Sediment compaction and fluid migration in the Makran
616   accretionary prism. *Journal of Geophysical Research: Solid Earth*, *94*(B6), 7387-7402.

617 Moore, J. C., & Vrolijk, P. (1992). Fluids in accretionary prisms. *Reviews of Geophysics, 30*(2),

618   113-135.

619 Morley, C. K., von Hagke, C., Hansberry, R. L., Collins, A. S., Kanitpanyacharoen, W., & King, R.

620   (2017). Review of major shale-dominated detachment and thrust characteristics in the

621   diagenetic zone: Part I, meso-and macro-scopic scale. Earth-Science Reviews, 173, 168–228.

622   https://doi.org/10.1016/j.earscirev.2017.07.019

623 Mostardini, F., & Merlini, S. (1986). Appennino centroemeridionale. Sezioni geologiche e proposta

624   di modello strutturale. Memorie della Societa Geologica Italiana, 35, 177–202.

625 O'Neil, J. R., Clayton, R. N., & Mayeda, T. K. (1969). Oxygen isotope fractionation in divalent

626   metal carbonates. *The Journal of Chemical Physics, 51*(12), 5547-5558.

627 Ogata, K., Pini, G. A., Carè, D., Zélic, M., & Dellisanti, F. (2012). Progressive development of

628   block-in-matrix fabric in a shale-dominated shear zone: Insights from the Bobbio

629   Tectonic Window (Northern Apennines, Italy). Tectonics, 31, TC1003. https://

630   doi.org/10.1029/ 2011TC002924

631 Raimbourg, H., Augier, R., Famin, V., Gadenne, L., Palazzin, G., Yamaguchi, A., & Kimura, G.

632   (2014). Long-term evolution of an accretionary prism: The case study of the Shimanto Belt,

633   Kyushu, Japan. *Tectonics, 33*(6), 936-959.

634 Renard, F., Ortoleva, P., & Gratier, J. P. (1997). Pressure solution in sandstones: influence of clays

635   and dependence on temperature and stress. *Tectonophysics, 280*(3-4), 257-266.

636 Sgrosso, I. (1974). I rapporti tra la piattaforma carbonatica Campano-Lucana e la piattaforma

637   Abruzzese-Campana al Monte Massico (Caserta). Bollettino della Società Geologica Italiana,

638   93(4), 1197–1209.

639 Smeraglia, L., Aldega, L., Billi, A., Carminati, E., Di Fiore, F., Gerdes, A., ... & Vignaroli, G.

640   (2019). Development of an Intrawedge Tectonic Mélange by Out-of-Sequence Thrusting,

641   Buttressing, and Intraformational Rheological Contrast, Mt. Massico Ridge, Apennines, Italy.

642   *Tectonics, 38*(4), 1223-1249.

643   Tavani, S., Storti, F., Lacombe, O., Corradetti, A., Muñoz, J. A., & Mazzoli, S. (2015). A review of
644   deformation pattern templates in foreland basin systems and fold-and-thrust belts:
645   Implications for the state of stress in the frontal regions of thrust wedges. *Earth-Science*
646   *Reviews*, *141*, 82-104.

647   Tesei, T., Collettini, C., Viti, C., & Barchi, M. R. (2013). Fault architecture and deformation
648   mechanisms in exhumed analogues of seismogenic carbonate-bearing thrusts. *Journal of*
649   *Structural Geology*, *55*, 167-181.

650   Toussaint, R., Aharonov, E., Koehn, D., Gratier, J. P., Ebner, M., et al. (2018). Stylolites: A review.
651   *Journal of Structural Geology 114*, 163-195.

652   Vannucchi, P., & Bettelli, G. (2002). Mechanism of subduction accretion as implied from the
653   broken formations in the Apennines, Italy. Geology, 30(9), 835–
654   838. https://doi.org/10.1130/0091-7613(2002)030<0835:MOSAAI>2.0.CO;2

655   Vannucchi, P., Remitti, F., & Bettelli, G. (2008). Geological record of fluid flow and seismogenesis
656   along an erosive subducting plate boundary. Nature, 451(7179), 699–
657   703. https://doi.org/10.1038/nature06486

658   Vannucchi, P., Remitti, F., Bettelli, G., Boschi, C., & Dallai, L. (2010). Fluid history related to the
659   early Eocene-middle Miocene convergent system of the Northern Apennines
660   (Italy): Constraints from structural and isotopic studies. Journal of Geophysical
661   Research, 115, B05405. https://doi.org/10.1029/2009JB006590

662   Vezzani, L., Festa, A., & Ghisetti, F. C. (2010). Geology and tectonic evolution of the
663   Central-Southern Apennines, Italy, Special Paper (Vol. 469, pp. 1–58). America: Geological
664   Society. https://doi.org/10.1130/2010.2469

665   Vitale, S., & Ciarcia, S. (2018). Tectono-stratigraphic setting of the Campania region (southern
666   Italy). Journal of Maps, 14(2), 9–21. https:// doi.org/10.1080/17445647.2018.1424655

667   Vitale, S., Prinzi, E. D., Ciarcia, S., Sabbatino, M., Tramparulo, F. D. A., & Verrazzo, G. (2018).
668   Polyphase out-of-sequence thrusting and occurrence of marble detritus within the wedge-top

669   basin deposits in the Mt. Massico (southern Apennines): Insights into the late

670   Miocene tectonic evolution of the central Mediterranean. International Journal of Earth

671   Sciences. https://doi.org/10.1007/s00531-018-1664-0

672   Vrolijk, P., Myers, G., & Moore, J. C. (1988). Warm fluid migration along tectonic melanges in the

673   Kodiak accretionary complex, Alaska. *Journal of Geophysical Research: Solid Earth*,

674   *93*(B9), 10313-10324.

675   Woodcock, N. H., Miller, A. V. M., & Woodhouse, C. D. (2014). Chaotic breccia zones on the

676   Pembroke Peninsula, south Wales: Evidence for collapse into voids along dilational faults.

677   *Journal of Structural Geology*, *69*, 91-107.

678

679   **Figure Captions**

680   **Figure 1. (a)** Simplified geological map of the central-southern Apennines (Italy) showing main

681   thrusts and location of the study area. **(b)** Schematic geological cross-section through

682   the central-southern Apennines (modified after Mostardini and Merlini, 1986). (c)

683   Geological cross-section through the Mt. Massico ridge (i.e., the study area).

684

685   **Figure 2. (a)** Detailed geological map of the southwestern part of the Mt. Massico ridge with

686   location of key outcrops where the tectonic mélange is exposed. Schmidt nets

687   (lower hemisphere) showing the attitude of S-C planes with related slip vectors within the

688   tectonic mélange. Modified after Smeraglia et al. (2019) **(b)** Geological cross-sections

689   across the Mt. Massico ridge.

690

691   **Figure 3.** Outcrop-scale structural features of the Mt. Massico tectonic mélange. **(a,b)** The poorly

692   deformed clastic deposits showing bedding and incipient foliation. Note folded strata and

693   low-displacement faults showing ramp and flat geometry. **(c)** The moderately deformed zone

694   showing competent strata (i.e. sandstones and calcarenites interbeds) characterized by pinch-

695   and-swell and boudine-like geometries. **(d)** Relict of competent strata. **(d)** Detail of competent

696   strata (Fig. 3c) showing veins perpendicular to bedding and S-C foliation. **(f,g)** The

697   strongly deformed part of the tectonic mélange showing S-C foliation within marls and shale

698   and relict of competent strata (limestones and sandstones) showing sigmoidal shapes. **(h)**

699   Relict of competent limestones showing stylolites along S- and C-planes. Inset shows the

700   Schmidt nets (lower hemisphere) showing the attitude of S-C planes with related slip vectors.

701

702   **Figure 4.** Outcrop-scale structural features of the Mt. Massico tectonic mélange. **(a-c)** The strongly

703   deformed part of the tectonic mélange characterized by S-C and S-CC' tectonites within marls

704   and shale and relict of competent strata (limestones and sandstones) showing sigmoidal

705   shapes. **(d)** Relict of competent limestones showing a pervasive network of calcite veins. **(e-**

706   **h)** Inherited competent (limestones) olistoliths scattered within the weak (marls and shale)

707   scaly foliation, generating the block-in-matrix fabric typical of tectonic mélange. **(h)**

708   Contorted and convoluted foliation within the S-C tectonite.

709

710   **Figure 5.** High-resolution hand sample scan of relicts of competent limestones showing sigmoidal

711   shapes. Stylolites are aligned along S-, C- and C'-planes. Calcite veins are oriented parallel,

712   perpendicular, and/or oblique with respect to stylolites. No stylolites affecting calcite veins

713   and calcite veins cutting through stylolites occur.

714

715   **Figure 6.** Microstructures from the tectonic mélange. **(a-c)** Stylolites affecting host rock relicts and

716   calcite veins. Note the insoluble materials (clays and oxides) filling up to 1-mm thick

717   dissolution seams. **(d,e)** Fibrous veins characterized by fibrous calcite crystals with long axis

718   oriented roughly parallel to stylolites. Note stylolites affecting fibrous veins. **(f)** Fibrous

719   crystals developed along stylolites jogs along C-plane. Fibrous crystals with long axis

720   oriented roughly parallel to stylolites.

721

Figure 7. Microstructures from the tectonic mélange. **(a,b)** Fibrous veins characterized by fibrous calcite crystals with long axis oriented perpendicular to stylolites. Note that this type of fibrous veins develop within stylolites. **(c,d,e,f)** Blocky veins characterized by blocky calcite crystals. Blocky veins are oriented parallel, perpendicular, and/or oblique respect to stylolites. Note stylolites affecting blocky veins and mutual crosscutting relationships between blocky veins.

728

Figure 8. (a) $\delta^{13}C$ (‰ V-PDB) versus $\delta^{18}O$ (‰ V-SMOW) diagram from blocky and fibrous veins and host rocks in the Mt. Massico tectonic mélange. Notice the average $\delta^{18}O$ depletion of ~4‰ between mélange-related mineralizations and host rock. **(b)** Oxygen isotope fractionation during equilibrium precipitation: $\delta^{18}O$ of fault-related mineralizations and paleofluid compositions (curves) as a function of temperature. The $\delta^{18}O$ calculated paleofluid compositions (between 9‰ and 14‰) indicate strong ^{18}O exchange with the local limestone host rock. Notice that warmer fluids have similar $\delta^{18}O$ paleofluid composition suggesting that the same paleofluid was the source for calcite precipitation at increasing temperatures and depths. **(c)** Temperature (°C, clumped isotopes) versus age (My, U-Pb dating, data from Smeraglia et al., 2019) diagram for three dated veins. Notice the increase in paleofluid temperature with decreasing ages, which indicates progressive tectonic burial during discontinuous thrust sheet emplacement through time. **(d)** $^4He/^{20}Ne$ ratio versus $^3He/^4He$ (R/Ra) ratio diagram. Note that the calcite veins are in the range of R/Ra values typical of crustal fluids of the central Apennines.

743

Figure 9. (a) Large-scale tectonic setting of the Apennine subduction (modified after Scrocca et al., 2005) and location of the Mt. Massico structure within the accretionary prism. **(b-c)** Simplified sketch showing the main sedimentary and tectonic events in the Mt. Massico area

747 (Modified after Smeraglia et a., 2019): **(b)** During late Tortonian-early Messinian

748 times, orogenic compression generated a fault propagation anticline located in the

749 northeastern part of the Mt. Massico ridge, juxtaposing pre-orogenic limestones in the

750 hangingwall with syn-orogenic Tortonian sandstones in the footwall. **(c)** During late

751 Messinian-early Pliocene times, out-of-sequence thrusting occurred and a ~3,300 m-thick

752 stack of imbricate thrust sheets thrust onto the Tortonian-lower Messinian clastic

753 deposits and calcarenites. At this stage the tectonic mélange develop at the base of the

754 clastic deposits. Notice that remnants of such thrust sheets are located in the Mt. Petrino area

755 (Fig. 2).

756 **Figure 10.** Simplified evolution of the Mt. Massico tectonic mélange (See Fig. 10b,c for the

757 structural location of the evolution scheme). **(a)** During the early deformation stage,

758 veins perpendicular to bedding develop within the clastic deposits in response to far field

759 tectonic stress. **(b)** Initial shortening affect the clastic deposits generating a weak scaly

760 foliation parallel respect to bedding (see Fig. 3a,b). **(c)** Progressive shortening generated S-C

761 fabric and boudinage of competent bedding (limestones and sandstones). **(d)** During the

762 late stage of deformation, the strongly deformed tectonic mélange develop. In particular,

763 pervasive S-C tectonites develop within the weak (marls and shale) matrix and relicts of

764 competent strata are deformed generating scattered clasts with sigmoidal shape. Notice that

765 hemipelagic marls are scraped off and mixed within the tectonic mélange, while the

766 underlying Meso-Cenozoic limestones are not deformed. The inset shows the different type

767 of veins within the mélange (blocky and fibrous) and their structural position respect to

768 stylolites.

769 **Figure 11.** Schematic evolutionary model for mélange-related veins evolution through time. Notice

770 alternate cycles of mutually overprinting brittle (fracturing/veining) and ductile (pressure-

771 solution and stylolites generation) processes.

772

773   **Figure S1. (a)** ^{40}Ar concentration versus age diagram. Notice that there is no correlation between

774   ^{40}Ar concentration and ages of dated veins. **(b)** ^{4}He concentration versus age diagram. Notice

775   that there is no correlation between ^{4}He concentration and ages of dated veins. **(c)** ^{3}He

776   concentration versus age diagram. Notice that there is no correlation between ^{3}He

777   concentration and ages of dated veins. **(d)** ^{3}He/^{4}He ratio (R/Ra) versus age diagram. Notice

778   that there is no correlation between ^{3}He/^{4}He ratio (R/Ra) and ages of dated veins.

a (map, upper panel)

Inset map:
Central-southern Apennines
Adriatic foreland
Rome
Tyrrhenian sea
Ionian sea

Gran Sasso
Morrone
Majella
Apennines external front
Marsica
Simbruini Mts.
Ernici Mts.
Volsci Mts.
Roccamonfina volcano
Matese Mts.
Garigliano Plain
Volturno Plain
Massico Mt. ridge
Ariano Basin

Legend:
Quaternary deposits
Volcanic deposits
Pliocene deposits
Syn-orogenic deposits (Miocene)
Ligurian accretionary complex (Jurassic-Lower Miocene)
Lagonegro-Molise Basin Unit (Triassic-Miocene)
Apennine platform unit (Triassic-Miocene)
Shallow water carbonates
Margin to pelagic carbonates
Thrust   Extensional fault

25 km

C – D cross section

C SW — Study area
Tectonic mélange
Mt. Massico ridge
NE | W
D E
1000
500
0 m
Middle-Upper Miocene clastic succession
Meso-Cenozoic carbonates
Tortonian sandstones
1 km

b (cross section A–B, lower panel)

A   Volsci Mts.   Simbruini-Ernici Mts.   Marsica   Majella-Morrone   B
km 0
5
10

25 km

Thrust
Extensional fault
Continental deposits (Plio-Quaternary)
Sandstones, marls, and claystones (Miocene)
Shallow water carbonates (Jurassic-Miocene)
Margin to pelagic carbonates (Jurassic-Miocene)
Dolostones (Triassic)
Crystalline rocks (Paleozoic)

Legend (stratigraphic column, left):

Debris (Holocene)

Ignimbrites (Pleistocene)

Calcarenites (Early Messinian) ~200 m

Siliciclastic/ carbonaticlastic deposits (Caiazzo Fm. Tortonian-early Messinian) ~450 m

Olistolith

Increasing tectonic deformation

Tectonic mélange ~150 m

Hemipelagic marls (Longano Fm. Serravallian) ~1-3 m

Bryozoan-rich limestones (Cusano Fm. Serravallian) ~50 m

Limestones (Up. Cretaceous)

Limestones (Lo. Cretaceous)

not to scale

Inset map legend:

Sandstones, marls and claystones
Limestones and dolostones
Volcanic deposits (Roccamonfina)
Slope debris deposits

Garigliano Plain

Massico Mt. range

Study area

Mondragone

Volturno Plain

Main map (a):

Fig. 7

Tectonic mélange boundary

San Sebastiano

Fig. 3d-h

Fig. 4a-h

Mt. Costa al sole

Mt. Malagna

Tectonic mélange boundary

Mt. Cicoli

Fig. 3a-c

Mt. Crestegallo

Mt. Petrino

1 km

a

Tectonic mélange kinematics:

n=263   n=143

σ3   σ1   σ2

Poles to S-plane
Poles to C-plane
Average S-planes
Average C-planes
C-planes
S-planes

Mappable Olistolith

Inferred fault
Transpressional fault
Extensional fault
Anticline axis
Syncline axis

Bedding attitude and dip

Tectonic transport direction

Moderately deformed zone

Cross-section trace

Cross-section (b):

400
0
-400
m

A   Mt. Petrino   Klippe   Tectonic mélange   A'

?   ?   ?   ?

1 km

B   Mt. Costa al Sole   Tectonic mélange   B'

500
0
-500
m

?   ?   ?

1 km

b

a S ... N
Marls and shales interbeds — Dismembered bedding
Incipient foliation
Bedding (sandstones)
50 cm

b S ... N
Marls and shales interbeds
Bedding (sandstones)
Low-displacement fault
50 cm

c S ... N
Bedding boudinage (competent strata)
Scaly foliation in weak layers (marls and shale interbeds)

d W ... E
Fig. 3e
Preserved competent bedding (limestones and sandstones)
Bedding
Bedding

e W ... E
Sigmoids of deformed bedding
C
S
C'
Stylolite
C
S
Veins perpendicular to bedding
Preserved bedding (calcarenite)
10 cm

f E ... W
S-C tectonites
Relict of competent bedding (sandstones)
S
C
Sandstone block
10 cm

g E ... W
S-C tectonites
S
C
Relict of competent bedding, Fig. 5 (limestone)
S
C
10 cm

h E ... W
S-C tectonites
C
Stylolite
S
n=19
S-plane
C-plane
Relict of competent bedding, Fig. 5 (limestone)
5 cm

(a) W — S-C tectonites — E; S, C

(b) W — S-CC' tectonites — E; C, S, S, C, S; Relict of competent bedding, Fig. 5 (limestone); S-plane, C-plane, n=22; 20 cm

(c) W — S-C tectonites — E; C, S; Relict of competent bedding, Fig. 5 (limestone); S-plane, C-plane, n=67; 20 cm

(d) W — S-C tectonites — E; Relict of competent bedding, Fig. 5 (limestone); Calcite veins; 5 cm

(e) W — E; Inherited limestone olistolith (competent block); Block-in-matrix fabric

(f) SE — NW; Scaly foliation; Inherited limestone olistolith (competent block); Block-in-matrix fabric; Deformed sandstones, marls, and shales (weak matrix)

(g) W — E; Inherited limestone olistolith (competent block); Block-in-matrix fabric; Scaly foliation (weak matrix); 20 cm

(h) W — S-C tectonites — E; Contorted foliation; 5 cm

Relicts of competent bedding

E — W

C plane

Veins aligned parallel to stylolites

Maximum shortening direction

C plane

S plane

S plane

C plane

Stylolites

Veins perpendicular or oblique respect to stylolites

5 cm

E — W

C plane

Stylolites

Maximum shortening direction

C plane

Vein along C plane

Veins cutting across stylolites

S plane

S plane

Veins aligned parallel to stylolites

5 cm

E — W

C plane

Maximum shortening direction

C plane

C plane

Veins perpendicular or oblique respect to stylolites

C' plane

S plane

C' plane

S plane

Veins aligned parallel to stylolites

5 cm

a — Stylolite, Fibrous vein, Fibrous vein, Host rock, Fibrous vein; 250 μm

b — Stylolite, Fibrous vein, Stylolite; 250 μm

c — Fibrous vein, Host rock, Blocky vein, Host rock, Blocky vein, Fibrous vein, Stylolite; 250 μm

d — Host rock, Blocky vein, Fibrous vein, Host rock, Stylolite, Fibrous vein; 250 μm

e — Host rock, Stylolite with teeth-shaped morphology, Blocky vein; 250 μm

f — Host rock, Blocky vein, Stylolite, Blocky vein; 250 μm

a Large-scale tectonic setting of the study area

SW

NE

Fig. 9b

0 km

10 km

Crust

20 km

30 km

25 km

40 km

appenninic slab

50 km

Lagonegro-Molise Basin Unit (Triassic-Miocene)

Internal and deformed apenninic nappes

Carbonate deposits (Triassic-Miocene)

Undifferentiated Plio-Pleistocene deposits

Syn-orogenic deposits (Miocene)

Thrust

Extensional fault

b

late Tortonian-early Messinian

clastic deposits

Hemipelagic marls

Accretionary wedge

Fig. 10a

Inactive thrust

Active thrust

Tortonian sandstones

Not to scale

late Messinian(?)-early Pliocene(?)

Folding of early Messinian clastic deposits

Fig. 10b-d

Out-of-sequence thrusts and imbicate thrust sheets

Tectonic mélange along the base of clastic deposits

Early deformation stage
(retained fluids in permeable layers)

a)

Meso-Cenozoic limestones

Fluid-saturated layers

Poorly deformed clastic deposits
(initial development of fluid overpressure)

b)

Shortening

Moderately deformed tectonic mélange
(overpressured fluid expulsion)

c)

S-C fabric

Boudinage of competent bedding

Strongly deformed tectonic mélange
(overpressured fluid expulsion)

d)

Block-in-matrix fabric

Relicts of Hemipelagic marls (Fig. 2a)

Sandstones

Limestones

Marls and shale

Hemipelagic marls

Exotic olistolith

Clay dehydration

Relicts of competent bedding

Veins inherited from early deformation pahse

Scaly foliation

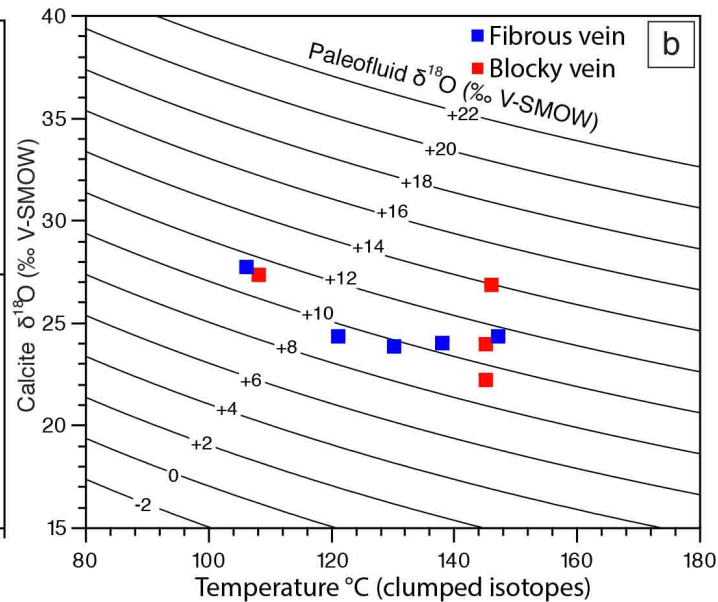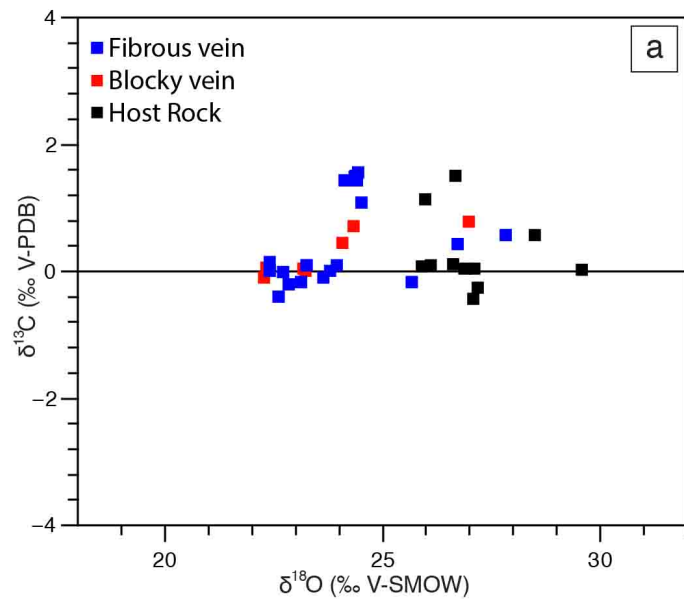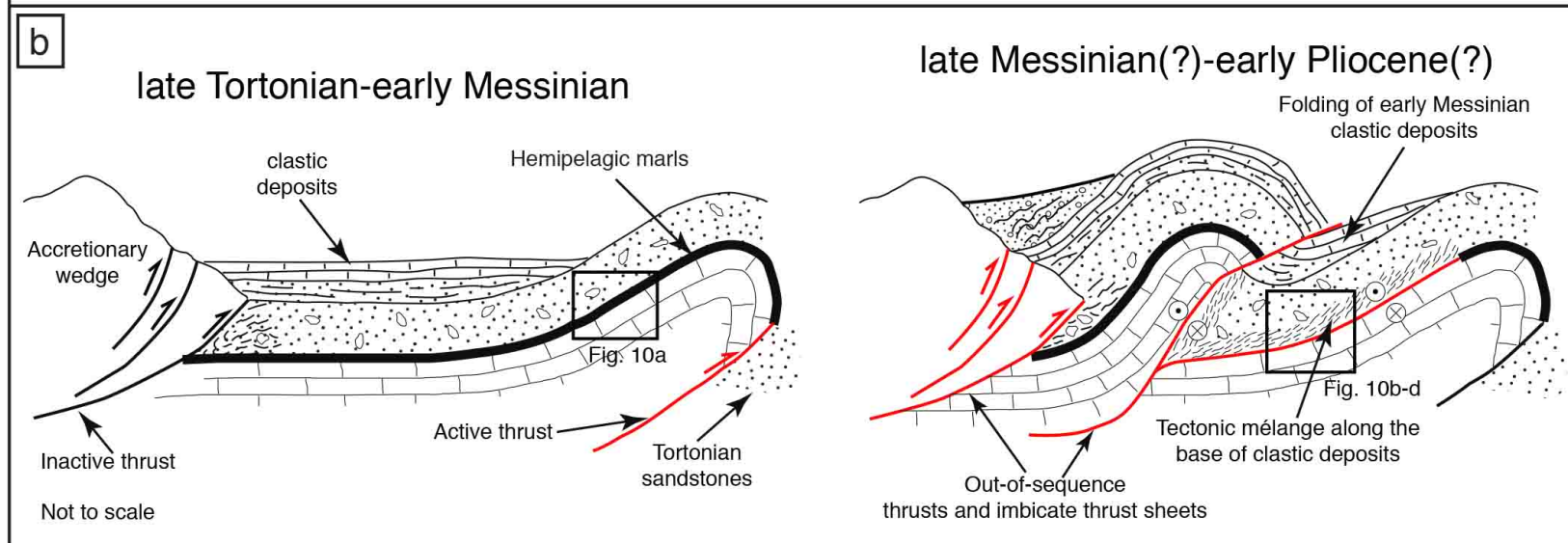S-plane (pressure-solution cleavage)

C-plane

Fluid expulsion

Fibrous vein (1) and slickenfiber (2)
micrometer-thick and multiple crack-and-seal events

Blocky vein
single crack-and-seal event

Stylolite

Stylolite step
Stylolite activated as shear plane

Strongly deformed tectonic mélange (Fig. 10d
(overpressured fluid expulsion)

Clay
dehydration

Fluid expulsion

Veins development within the tectonic mélange

Cycles of mutually overprinting brittle and ductile processes
assisted by overpressured fluids

Future
dissolution zone

**Brittle-ductile
deformation**

**Assisted by
fluid
overpressure**

**Assisted by
fluid
overpressure**

**Brittle-ductile
deformation**

Reworking/rotation of
pre-existing veins

**Brittle
deformation**

**Assisted by
fluid
overpressure**

Host rock
lense

Crackle-like texture

Stylolite   Inherited
vein   Veins related to
pressure-solution   Veins related to episodic event
of fracturing/brecciation
(Crackle-like texture)

Declaration of interests

The authors declare that they have no known competing financial interests or personal relationships that could have appeared to influence the work reported in this paper.
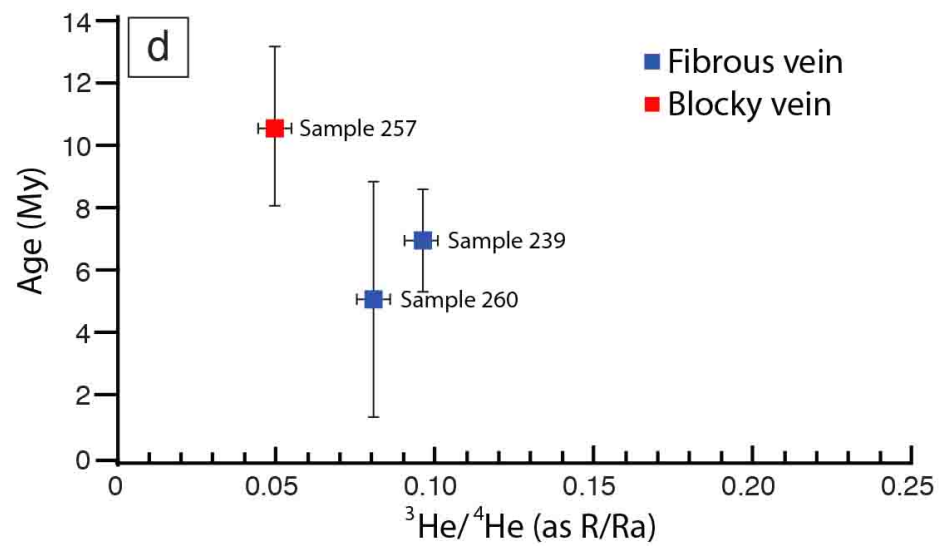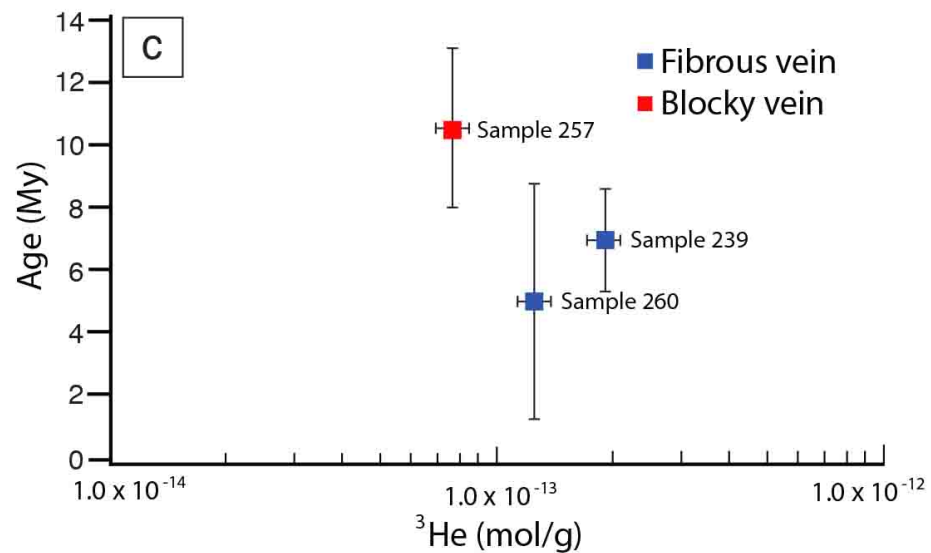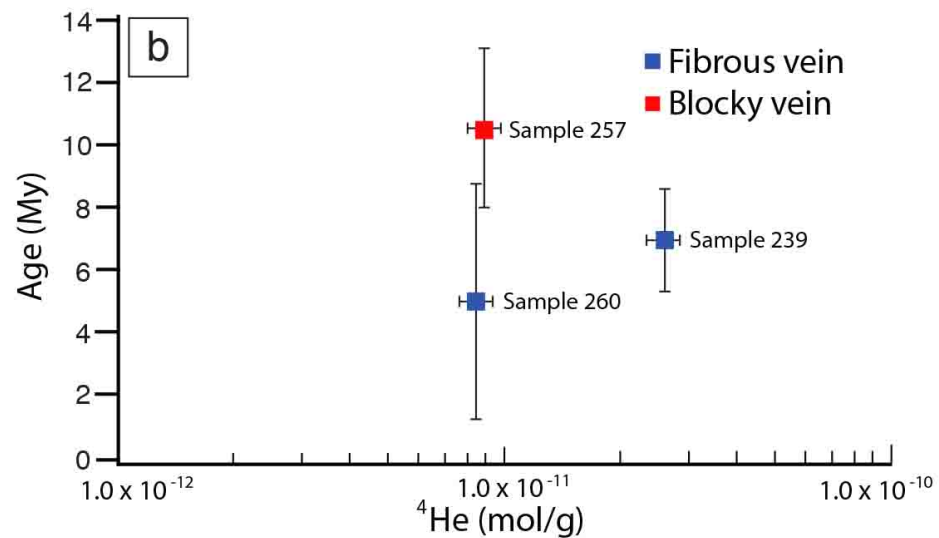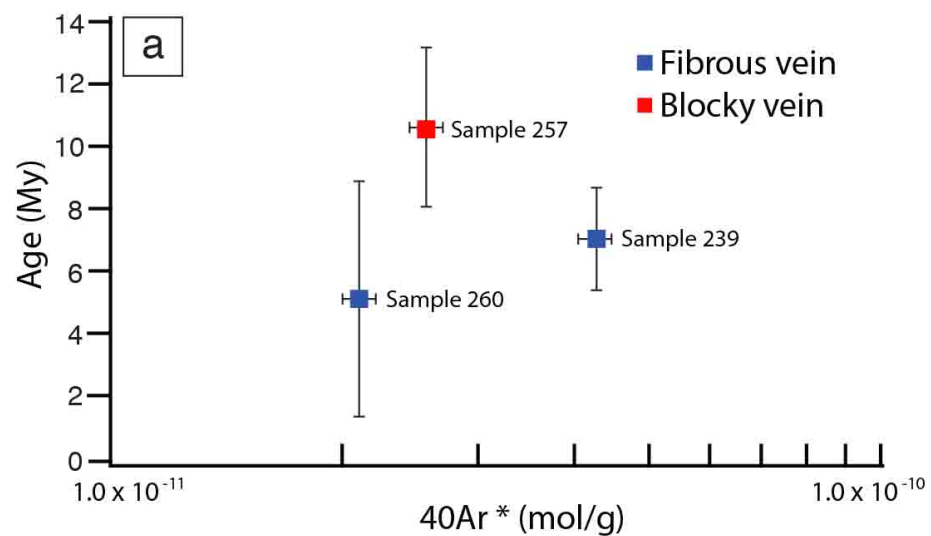
Locality	Number	Sample type	$\delta^{13}C$ ‰ (V-PDB)	$\delta^{18}O$ ‰ (V-SMOW)
N 41°09'59'' E 13°53'03''	242	Blocky vein	0.45	24.05
N 41°09'59'' E 13°53'03''	234	Blocky vein	0.73	24.31
N 41°09'59'' E 13°53'03''	233-2	Blocky vein	0.80	26.97
N 41°09'59'' E 13°53'03''	238-1	Fibrous vein	-0.38	22.61
N 41°09'59'' E 13°53'03''	259	Fibrous vein	0.59	27.82
N 41°09'59'' E 13°53'03''	235	Fibrous vein	0.44	26.70
N 41°09'59'' E 13°53'03''	237-1	Fibrous vein	1.09	24.51
N 41°09'59'' E 13°53'03''	237-2	Fibrous vein	1.56	24.42
N 41°09'59'' E 13°53'03''	237-3	Fibrous vein	1.45	24.40
N 41°09'59'' E 13°53'03''	237-4	Fibrous vein	1.50	24.35
N 41°09'59'' E 13°53'03''	254-1	Fibrous vein	-0.09	23.62
N 41°09'59'' E 13°53'03''	254-2	Fibrous vein	-0.16	25.65
N 41°09'59'' E 13°53'03''	254-3	Fibrous vein	-0.19	22.84
N 41°09'59'' E 13°53'03''	260-2	Fibrous vein	0.11	23.24
N 41°09'59'' E 13°53'03''	260-3	Blocky vein	0.06	23.17
N 41°09'59'' E 13°53'03''	260-4	Blocky vein	0.01	23.22
N 41°09'59'' E 13°53'03''	260-5	Fibrous vein	0.11	23.94
N 41°09'59'' E 13°53'03''	260-8	Fibrous vein	0.02	23.79
N 41°09'59'' E 13°53'03''	265	Fibrous vein	0.16	22.40
N 41°09'59'' E 13°53'03''	265-2	Fibrous vein	0.00	22.69
N 41°09'59'' E 13°53'03''	265-3	Fibrous vein	0.01	22.40
N 41°09'59'' E 13°53'03''	265-5	Blocky vein	-0.08	22.27
N 41°09'59'' E 13°53'03''	265-6	Blocky vein	0.01	22.35
N 41°09'59'' E 13°53'03''	265-7	Blocky vein	0.07	22.31
N 41°09'59'' E 13°53'03''	266	Fibrous vein	1.44	24.11
N 41°09'59'' E 13°53'03''	266 bis	Fibrous vein	-0.16	23.10
N 41°09'59'' E 13°53'03''	266 S-plane	Fibrous vein	1.52	24.38
N 41°09'59'' E 13°53'03''	HR 1	Host rock	0.58	28.48
N 41°09'59'' E 13°53'03''	HR 2	Host rock	1.15	25.97
N 41°09'59'' E 13°53'03''	HR 3	Host rock	0.04	29.56
N 41°09'59'' E 13°53'03''	HR 4	Host rock	-0.42	27.06
N 41°09'59'' E 13°53'03''	HR 5	Host rock	0.13	26.60
N 41°09'59'' E 13°53'03''	HR 6	Host rock	0.05	27.10
N 41°09'59'' E 13°53'03''	HR 7	Host rock	0.06	26.85
N 41°09'59'' E 13°53'03''	HR 8	Host rock	0.09	25.89
N 41°09'59'' E 13°53'03''	HR 9	Host rock	1.52	26.65
N 41°09'59'' E 13°53'03''	HR 10	Host rock	-0.24	27.16
N 41°09'59'' E 13°53'03''	HR 11	Host rock	0.11	26.08

Table S1. Summary of $\delta^{18}O$- and $\delta^{13}C$-isotopes analyses on mélange-related mineralizations

Sample type	Replicates	$\delta^{13}C$ V-PDB	$\delta^{13}C$ V-PDB SD	$\delta^{18}O$ V-PDB	$\delta^{18}O$ V-PDB SD	$\delta^{18}O$ V-SMOW	$\Delta47$ CDES	$\Delta47$ CDES SD	$\Delta47$ CDES SE	Average T °C	SD	SE	68% Conf Level	95% Conf Level	$\delta^{18}O$ paleofluid (VSMOW) (O'Neil et al.. 1969)
Blocky vein	10	0.78	0.01	-3.89	0.02	26.91	0.424	0.027	0.009	146	21.6	6.8	7.2	15.4	13.7
Blocky vein	11	0.44	0.02	-6.73	0.04	23.98	0.426	0.026	0.008	145	23.9	7.2	7.6	16.1	10.8
Blocky vein	8	0.67	0.02	-3.41	0.04	27.41	0.477	0.027	0.009	108	15.5	5.5	5.9	13.0	10.9
Blocky vein	13	0.02	0.11	-8.38	0.24	22.28	0.426	0.027	0.007	145	21.5	6.0	6.2	13.0	9.1
Fibrous vein	7	1.57	0.02	-6.32	0.03	24.41	0.424	0.026	0.010	147	22.3	8.4	9.1	20.6	11.3
Fibrous vein	10	0.06	0.02	-6.32	0.03	24.40	0.457	0.023	0.007	121	14.7	4.6	4.9	10.5	9.1
Fibrous vein	11	0.59	0.03	-3.04	0.06	27.79	0.482	0.034	0.010	106	20.4	6.2	6.4	13.7	11.0
Fibrous vein	8	0.10	0.01	-6.83	0.03	23.88	0.449	0.025	0.008	130	17.7	6.2	6.7	14.8	9.4
Fibrous vein	10	1.53	0.01	-6.64	0.02	24.08	0.433	0.015	0.005	138	11.0	3.5	3.7	7.9	10.3

Table S2. Summary of clumped isotopes analyses. SD, Standard Deviation; SE, Standard Error; CDES

Sample	Weight (g)	^{4}He mol/g	^{4}He err	^{3}He mol/g	^{3}He err	^{20}Ne mol/g	^{20}Ne err	H$_2$O+CO$_2$ mol/g	N$_2$ mol/g	^{40}Ar mol/g	^{40}Ar err	^{40}Ar* mol/g	^{40}Ar* err	He/Ar	N$_2$/Ar	He/Ne	He/Ar*	Err	R/Ra	Rc/Ra	Err tot +/-	^{40}Ar/^{36}Ar	Error (%)
239	0,185	$2{,}59 \times 10^{-11}$	0,02	$3{,}38 \times 10^{-18}$	4,60	$2{,}68 \times 10^{-13}$	0,65	$8{,}28 \times 10^{-6}$	$6{,}67 \times 10^{-7}$	$1{,}84 \times 10^{-10}$	0,04	$4{,}26 \times 10^{-11}$	0,08	$1{,}41 \times 10^{-1}$	3633,289	96,5	0,61	0,1	0,10	0,09	0,004	388,88	0,07
260	0,112	$8{,}42 \times 10^{-11}$	0,01	$9{,}23 \times 10^{-19}$	5,76	$1{,}06 \times 10^{-13}$	0,69	$1{,}12 \times 10^{-6}$	$3{,}07 \times 10^{-7}$	$8{,}99 \times 10^{-11}$	0,07	$2{,}10 \times 10^{-11}$	0,16	$9{,}37 \times 10^{-2}$	3413,257	79,4	0,40	0,2	0,08	0,08	0,005	389,94	0,15
257	0,118	$8{,}91 \times 10^{-11}$	0,01	$6{,}04 \times 10^{-19}$	6,11	$1{,}73 \times 10^{-13}$	0,61	$2{,}58 \times 10^{-6}$	$4{,}25 \times 10^{-7}$	$1{,}38 \times 10^{-10}$	0,06	$2{,}57 \times 10^{-11}$	0,13	$6{,}48 \times 10^{-2}$	3092,841	51,7	0,35	0,1	0,05	0,05	0,003	367,29	0,12

Table S3. Summary of isotope data from fluid inclusions analysis of sin-tectonic calcite veins from the tectonic mélange

grain		207Pba (cps)	U (ppb)	Pb (ppb)	Th/U	206Pbd/238U	±2s (%)	207Pbd/206Pb	±2s (%)
A06	257	471600	1813	2050	1,45	0,6812	3,0	0,8316	0,29
A07		743113	2742	3190	1,59	0,6995	2,3	0,8354	0,26
A08		260035	1484	1140	1,75	0,4622	3,8	0,8341	0,36
A09		285988	1597	1222	1,33	0,461	3,8	0,8312	0,32
A10		337476	1242	1442	1,83	0,6985	3,7	0,833	0,31
A11		859984	2505	3710	1,34	0,8915	3,0	0,8333	0,26
A12		848268	2668	3655	1,04	0,825	2,4	0,8325	0,28
A13		848529	2950	3677	1,28	0,7508	2,8	0,8314	0,25
A14		178565	743	770	1,83	0,623	2,6	0,836	0,41
A15		289446	1019	1254	1,31	0,7413	2,9	0,8326	0,33
A16		600706	3321	2920	1,48	0,5291	12,8	0,8341	0,33
A17		39317	28	170	0,90	3,589	3,2	0,8401	0,83
A18		49523	41	216	0,27	3,142	4,4	0,8369	0,9
A19		26662	26	115	0,70	2,711	2,9	0,8369	1
A357	239	12788	285	65	0,02	0,1384	2,4	0,8223	1,2
A358		18181	191	96	0,02	0,303	2,8	0,8235	0,99
A359		14325	241	75	0,01	0,1893	2,6	0,8241	1,4
A360		10828	280	57	0,01	0,1228	2,4	0,8226	1,2
A361		10706	363	57	0,00	0,09543	2,5	0,8109	1,2
A362		10988	348	58	0,01	0,1019	2,9	0,8148	1,5
A363		12475	330	65	0,00	0,1201	2,2	0,8217	1,2
A364		17402	368	92	0,01	0,1525	2,6	0,8174	1,2
A365		15176	390	80	0,01	0,1241	2,2	0,824	1,4
A366		6761	174	36	0,04	0,1245	2,3	0,821	1,4
A367		8980	177	47	0,04	0,1606	2,6	0,8241	1,5
A368		4920	426	27	0,02	0,03843	2,7	0,8025	1,9
A369		4639	372	24	0,02	0,04009	2,9	0,8108	1,5
A370		5947	327	32	0,01	0,05904	2,5	0,8161	1,6
A371		9201	336	49	0,01	0,08899	2,3	0,8169	1,1
A372		9057	447	48	0,01	0,06531	2,2	0,8188	1,5
A373		6908	380	37	0,01	0,05856	2,6	0,8195	1,6
A374		7199	428	38	0,00	0,05435	2,4	0,8226	1,4
A375		5955	393	32	0,02	0,04907	2,7	0,813	1,5
A376		6757	314	36	0,02	0,06952	2,5	0,8158	1,7
A377		7776	396	42	0,01	0,06384	2,6	0,8122	1,6
A378		27871	67	148	0,09	1,339	2,3	0,8237	0,82
A379		36109	87	191	0,14	1,332	2,5	0,8282	0,66
A380		29563	77	157	0,08	1,237	2,5	0,827	0,79
A381		29869	62	155	0,08	1,511	2,2	0,8303	0,65
A382		6778	270	37	0,02	0,08265	2,7	0,816	1,4
A388		5744	357	31	0,02	0,05281	3,1	0,8086	1,7

A389		8213	359	44	0,01	0,07527	3,4	0,8178	1,3
A390		4465	466	24	0,00	0,03182	2,5	0,7943	1,6
A391		7002	296	38	0,00	0,07781	3,1	0,8133	1,9
A392		4777	310	26	0,01	0,05026	3,2	0,819	1,7
A393		4529	355	25	0,01	0,04272	2,6	0,8027	2,3
A394		5007	525	28	0,00	0,03264	2,6	0,7964	1,6
A395		6174	372	34	0,00	0,05504	2,5	0,8121	1,6
A396		6364	386	35	0,00	0,0553	2,4	0,8108	1,6
A397		7127	430	39	0,00	0,05461	2,3	0,8224	1,1
A398		6037	407	33	0,00	0,04976	2,6	0,8068	1,5
A279	260	13497	219	67	0,33	0,1848	5,4	0,8327	1,3
A280		5001	160	26	0,41	0,09853	3,6	0,8033	1,8
A281		5932	277	30	0,28	0,06634	4,0	0,8151	1,9
A282		4217	185	21	0,24	0,07005	3,4	0,8215	3
A288		2222	143	12	0,16	0,04938	4,1	0,7978	2,9
A289		2093	100	10	0,11	0,0627	3,5	0,8231	3
A290		4225	138	21	0,20	0,09378	3,8	0,8269	2,2
A291		2031	115	11	0,08	0,05615	3,3	0,8012	3,1
A292		3437	183	18	0,24	0,05916	2,6	0,8036	2,7
A293		2266	189	12	0,03	0,03706	3,3	0,8226	2,8
A294		2120	141	11	0,04	0,04753	4,1	0,8059	2,3
A295		2135	197	11	0,02	0,03456	2,8	0,7943	2,6
A296		3288	182	17	0,08	0,05596	4,8	0,8266	2,2
A297		1759	175	9	0,02	0,03171	3,6	0,8073	3,1
A298		1526	188	8	0,01	0,0265	3,3	0,7891	3,4
A299		1516	207	8	0,01	0,0253	3,2	0,7562	2,5
A300		2051	221	11	0,01	0,02958	4,8	0,7964	2,5
A301		3149	190	16	0,04	0,05305	3,5	0,7994	2,8
A302		3162	58	16	0,07	0,1711	2,6	0,8152	2,7
A303		5499	57	28	0,09	0,2944	2,9	0,8301	1,8
A304		1879	225	10	0,01	0,02713	3,2	0,7866	3,1
A305		2075	244	11	0,01	0,02725	3,9	0,7959	2,9
A306		3289	226	17	0,04	0,0464	4,5	0,8082	3,1
A307		1723	248	9	0,01	0,02306	3,2	0,7729	3,4
A308		2257	190	12	0,02	0,03743	3,2	0,813	3,2
A309		3923	20	20	1,77	0,602	3,9	0,8285	1,9
A310		3197	132	17	0,06	0,0771	4,4	0,809	2,7

Table S4. Summary of in situ U, Pb, and Th analyses of syn-tectonic calcite veins from the tectonic Mélange

Methods

Stable and Clumped isotopes

The stable and clumped isotope composition of the carbonates were determined at ETH Zürich using a Thermo Fisher Scientific MAT253 mass spectrometer coupled to a Kiel IV carbonate preparation device, following the method described in Schmid and Bernasconi (2010), Meckler et al. (2014), and Müller et al. (2017). The Kiel IV device included a PoraPakQ trap kept at -40°C to eliminate potential organic contaminants. Prior to each sample run, the pressure-dependent backgrounds were determined on all beams to correct for non-linearity effects in the mass spectrometer according to Bernasconi et al. (2013). During each run of the autosampler of 46 positions, 3 replicates each of 95-110 μg of different samples and 5 replicates the carbonate standards ETH-1, ETH-2, and 10 replicates of the standard ETH-3 were analyzed with the LIDI method (Müller et al. 2017). The samples were measured over a period of three weeks to avoid biases due to short-term variations in the performance of the instruments. All calculations and corrections were done with the software Easotope (John and Bowen, 2016) using the revised IUPAC parameters for ^{17}O correction as suggested by Daeron et al. (2016). Temperatures were calculated using the O'Neal et al. (1969) calibration recalculated using fully recalculated values of the ETH standards and of calibration samples as described in Bernasconi et al. (2018). The complete results are reported in Table S3 in relation to the carbon dioxide equilibrium scale (CDES) projected to an acid digestion temperature of 25°C.

Analytical technique for fluid inclusions

We determined the H_2O+CO_2, and N_2 content and the elemental and isotope composition of noble gases (He, Ne, and Ar) in fluid inclusions of Sample 239, Sample 257, and Sample 260 of calcite veins from Mt. Massico tectonic mélange. Samples were prepared and analyzed in the laboratories of Istituto Nazionale di Geofisica e Vulcanologia (INGV), Sezione di Palermo (Italy),

27   following the preparation and analytical protocols described in Smeraglia et al. (2018) and Rizzo et

28   al. (2019). Complete results are reported in Figs. 8d, S2 and Table S3.

29   H_2O+CO_2 in fluid inclusions have been extracted and quantified in a stainless steel crusher

30   during noble gas extraction, which gives a good indication of the moles of gaseous matrix of fluid

31   inclusions but does not completely preserve these species from adsorption and fractionation in

32   powders and stainless steel. In the first stage, part of the vein samples has been gently broken,

33   sieved with a diameter >1 mm mesh. The selected crystals were cleaned in an ultrasonic bath. The

34   portion of the selected sample material was weighed in an analytical balance, thus loaded into a

35   stainless-steel crusher baked for 48-72h at 120°C in order to put in ultra-high-vacuum conditions

36   (10^{-9} mbar). Fluid inclusions were released by a single-step (in-vacuum) crushing performed at

37   200 bar. The amount of material loaded for each analysis was ~0.1-0.2 g. This procedure is the most

38   conservative in order to minimize the contribution of cosmogenic ^3He and radiogenic ^4He possibly

39   grown/trapped in the crystal lattice (e.g., Hilton et al., 1993, 2002). The atmospheric component

40   was separated and quantified at the time of crushing by observing the following steps: immediately

41   after crushing, we read the total gas pressure ($N_2+O_2+H_2O+CO_2$+noble gases). Then, N_2+O_2+noble

42   gases were separated from the H_2O+CO_2 by using a "cold finger" immersed in liquid nitrogen (T= -

43   196 ° C) that allows freezing H_2O and CO_2. After this step, we checked again the total pressure for

44   quantifying the atmospheric component. Noble gases separated from H_2O and CO_2 were further

45   cleaned in an ultra-high vacuum (10^{-9} - 10^{-10} mbar) purification line, and all the species of the gas

46   mixture, except noble gases, were removed from four getters.

47   Helium (^3He and ^4He) and neon (^{20}Ne, ^{21}Ne and ^{22}Ne) isotopes were measured separately by

48   two different split-flight-tube mass spectrometers (Helix SFT-Thermo). The values of the $^3He/^4He$

49   ratio are expressed as R/Ra (where Ra is the $^3He/^4He$ ratio of air, which is equal to 1.39×10^{-6}). In

50   addition, due to the presence of air He contamination, the R/Ra values were corrected based on the

51   measured $^4He/^{20}Ne$ ratio (e.g., Sano et al., 1985) and are expressed as Rc/Ra values. However, the

52   corrected ratios show minimum to negligible differences respect to raw ^{3}He/^{4}He ratios. The

53   analytical uncertainty of He isotopic ratio is $\leq 6\%$, while that of ^{20}Ne/^{22}Ne is $<0.17\%$.

54   Argon isotopes (^{36}Ar, ^{38}Ar and ^{40}Ar) were analyzed by a multicollector mass spectrometer

55   (GVI Argus), with an analytical uncertainty $< 0.14\%$. The uncertainty in the determinations of He,

56   Ne, and Ar elemental contents was less than 0.1%. Typical blanks for He, Ne and Ar were $<10^{-15}$,

57   $<10^{-15}$ and $<10^{-14}$ mol, respectively, and are at least two orders of magnitude lower than analytical

58   signals of samples. Further details about the sample preparation and analytical procedures are

59   available in Rizzo et al. (2018, 2019) and Smeraglia et al. (2018).

60

61   **References**

62   Bernasconi S.M., Müller I. A., Bergmann K.D., Breitenbach S. F. M., Fernandez, A., Hodell D. A.,

63   Jaggi M., Meckler A.N. Millan I., and Ziegler M. (2018) Reducing uncertainties in carbonate

64   clumped isotope analysis through consistent carbonate-based standardization. *Geochemistry*

65   *Geophysics Geosystems* 19. https://doi.org/10.1029/2017GC007385

66   Bernasconi, S.M., Hu, B., Wacker, U., Fiebig, J., Breitenbach, S.F.M., Rutz, T., 2013. Background

67   effects on Faraday collectors in gas-source mass spectrometry and implications for clumped

68   isotope measurements. *Rapid Communications in Mass Spectrometry,* 27, 603–612.

69   doi:10.1002/rcm.6490

70   Breitenbach S.F.M, Mlenek-Vautravers, M.J., Grauel A.L., Bernasconi S.M. Müller, I.A., Rolfe, J.

71   Gázquez F., Greaves M. Elderfield, H. and Hodell, D.A. (in revision) Coupled Mg/Ca and

72   clumped isotope analyses of foraminifera provide consistent water temperatures. Geochimica

73   Cosmochimica Acta.

74   Dennis, K.J., Affek, H.P., Passey, B.H., Schrag, D.P., Eiler, J.M., 2011. Defining an absolute

75   reference frame for "clumped" isotope studies of CO_2. Geochimimica et Cosmochimica Acta,

76   75, 7117–7131. doi:10.1016/j.gca.2011.09.025.

Hilton, D.R., Fischer, T.P., Marty, B., 2002. Noble gases and volatile recycling at subduction zones. Rev. Min. and Geoch. 47, 319-370. https://doi.org/10.2138/rmg.2002.47.9.

Hilton, D.R., Hammerschmidt, K., Teufel, S., Friedrichsen, H. 1993. Helium isotope characteristics of Andean geothermal fluids and lavas. Earth Planet. Sci. Lett. 120, 265-282. https://doi.org/10.1016/0012-821X(93)90244-4.

John, C.M., Bowen, D., 2016. Community software for challenging isotope analysis: First applications of "Easotope" to clumped isotopes. *Rapid Communications in Mass Spectrometry,* 30, 2285–2300. doi:10.1002/rcm.7720

Kele, S., Breitenbach, S. F., Capezzuoli, E., Meckler, A. N., Ziegler, M., Millan, I. M., Kluge, T., Deak, J., Hanselmann, K., John, C.M., Yan, H., Liu, Z., Bernasconi, S.M. (2015). Temperature dependence of oxygen-and clumped isotope fractionation in carbonates: A study of travertines and tufas in the 6–95 °C temperature range. Geochimica et Cosmochimica Acta 168, 172-192. https://doi.org/10.1016/j.gca.2015.06.032.

Meckler, A.N., Ziegler, M., Millán, M.I., Breitenbach, S.F.M., Bernasconi, S.M., 2014. Long-term performance of the Kiel carbonate device with a new correction scheme for clumped isotope measurements. Rapid Comm. in Mass Spectrom. 28, 1705-1715.

Müller, I.A., Fernandez, A., Radke, J., Dijk, J. Van, Bowen, D., Schwieters, J., Bernasconi, S.M., 2017. Carbonate clumped isotope analyses with the long-integration dual-inlet (LIDI) workflow : scratching at the lower sample weight boundaries. *Rapid Communications in Mass , 2, 1057–1066. doi:10.1002/rcm.7878

O'Neil, J. R., Clayton, R. N., & Mayeda, T. K. (1969). Oxygen isotope fractionation in divalent metal carbonates. *The Journal of Chemical Physics*, *51*(12), 5547-5558.

Rizzo AL, Pelorosso B, Coltorti M, Ntaflos T, Bonadiman C, Matusiak-Małek M, Italiano F and Bergonzoni G (2018) Geochemistry of Noble Gases and CO_2 in Fluid Inclusions From Lithospheric Mantle Beneath Wilcza Góra (Lower Silesia, Southwest Poland). Front. Earth Sci. 6:215. doi: 10.3389/feart.2018.00215

103   Rizzo, A. L., Uysal, I. T., Mutlu, H., Ünal-İmer, E., Dirik, K., Yüce, G., et al. (2019). Geochemistry

104   of fluid inclusions in travertines from western and northern Turkey: Inferences on the role of

105   active faults in fluids circulation. Geochemistry, Geophysics, Geosystems,

106   20. https://doi.org/10.1029/2019GC008453

107   Sano, Y., Urabe, A., Wakita, H., Chiba, H., Sakai, H., 1985. Chemical and isotopic compositions of

108   gases in geothermal fluids in Iceland. Geoch. J. 19, 135-148.

109   https://doi.org/10.2343/geochemj.19.135.

110   Schmid, T.W., Bernasconi, S.M., 2010. An automated method for "clumped-isotope" measurements

111   on small carbonate samples. *Rapid Communications in Mass Spectrometry* , 24, 1955–1963.

112   doi:10.1002/rcm.4598.

113